Modelling strain rate and temperature dependent mechanical response of PMMAs at large deformation from below to above Tg

C.E. Federico, Jean-Luc Bouvard, Christelle Combeaud, N. Billon

Modelling strain rate and temperature dependent mechanical response of PMMAs at large deformation from below to above Tg

C. E. Federico [a,1], J.L. Bouvard [a], C. Combeaud [a], N. Billon [a,*]

[a] MINES ParisTech, PSL Research University, CEMEF – Center for materials forming, CNRS UMR 7635, CS 10207, rue Claude Daunesse 06904 Sophia Antipolis Cedex, France

Corresponding author: Noelle.billon@mines-paristech.fr

[1] Presently at: Luxembourg Institute of Science and Technology, L-4940 Hautcharage, Luxembourg.

Keywords

PMMA; viscoelasticity; hyperelasticity; time-temperature principle; mechanical behaviour; modelling

Abstract

The potential and the interest of the development of mechanical approach based on concepts issued from the physics of polymers, as well as of the use of the time temperature equivalence principle, are illustrated. To achieve that point, a revisited constitutive model [1], [2] was used to model the mechanical behaviour of amorphous PMMA with different molecular weights. The model accounts for the elastic contribution of an equivalent network which experiences inelastic mechanisms coming from the evolution of internal state variables when the polymer is deformed. The experimental database included non-monotonic tensile tests at targeted “equivalent strain rate at reference temperature” coupled with DIC for obtaining local boundary conditions. Model exhibited good capabilities to capture the mechanical response of the material at different temperatures and strain rates corresponding to material state ranging from the end of the glassy state to near-liquid state going through viscoelastic and rubbery regime. Analysis of the parameters allowed introducing empirical equations to consider the time/temperature dependence into the model. It was possible to pretty well reproduce the behaviour of PMMAs from rubbery like domains to their glassy state with one unique formalism and

one unique and of reduced number set of parameters. Effect of molar mass and crosslinking are discussed.

1 Introduction

To take advantage of polymer materials, it is of main importance to describe their mechanical behaviour in a specific manner and to understand how the mechanical behaviour varies with the polymer nature and its use conditions, especially close to the glass transition temperature, *Tg*. From this point of view, temperature, loading rate, entanglement and crosslink density greatly affect the mobility of the polymer chains, which bring strong evolution of the mechanical properties of the material.

In the literature, it is possible to find many works devoted to describe the mechanical behaviour of amorphous or semi crystalline polymers (see in example [3] for a review) using either phenomenological or physical routes. Despite sometimes good results in tensile and compression loadings, phenomenological models [4]–[10] still have difficulties in predicting the mechanical response over a wide range of temperature and/or strain rate and particularly for cyclic loading. Some studies have attempted to describe the complex mechanical behaviour of amorphous polymers under large deformation by combining phenomenological and physical approaches. Examples can be found in constitutive modelling proposed by Hasan et al. [11], Muliana et al. [12], Guo et al. [13], Yu et al. [14], Li et al. [15], Gu et al. [16] and Praud et al. [17] which displayed satisfactory results for monotonic and non-monotonic loadings. However, these models were applied up to true strains of 20%, leaving the domain of larger strain level unexplored.

Works from Buckley et al. [18], [19] on PET, Dooling et al. [20] on high molecular weight PMMAs, Sweeney et al. [21] on PP and Dupaix and Boyce [22] on amorphous PETG, proposed constitutive models which aim at capturing the rate-dependent behaviour at temperatures near the glass transition by accounting entropic and viscous effects on the polymer network. These models captured the mechanical behaviour of polymers at large deformation under monotonic uniaxial and biaxial testing at increasing temperature. However, they were not developed for reproducing the response during unloading stage. Ayoub et al. [23] proposed a physically-based inelastic model for reproducing loading-unloading large deformation tests on HDPE. The inelastic mechanisms were described by using two parallel elements: a viscohyperelastic network resistance and a viscoelastic-viscoplastic intermolecular resistance. The network resistance was constituted by the eight-chain rubber model [24] and an inelastic shear strain rate given by Bergstrom and Boyce [25], [26]. The intermolecular resistance was composed by an initial elastic response followed by a non-linear transition to the

inelastic flow (Colak [27]). The nonlinear unloading behaviour was well described by this model, which is a remarkable achievement. However, the stress during the loading stage was underestimated up to a strain of 90% and beyond this deformation, stresses were highly overestimated. Srivastava, Anand, Ames et al. [28]–[30] introduced macroscopic internal state variables to represent important features of the microstructure resistance to plastic flow and strain hardening. Intermolecular resistance was described by nonlinear springs and thermally activated dashpots in parallel with another nonlinear spring. The molecular network resistance was described using a phenomenological form of the free energy function (see Gent [31]) and the viscous part was included by using evolution equation for internal state variables. The model is in good agreement with the experimental results of amorphous polymers at large deformation levels from room temperature to approximately 50 °C above the glass transition temperature. Despite of the model accuracy, the number of parameters is quite high which makes the identification of the model parameter more demanding. More recently Wang et al. [59] developed a viscoelastic-viscoplastic model based on intramolecular interaction and intermolecular interaction they decomposed into chain entanglement and secondary bonding such as van der Waals interactions. The model shows its capability to capture the polymer response under cyclic loading as well as stress relaxation and strain recovery. We can also refer to [60] regarding the development of a thermomechanical elastoviscoplastic model that showed capabilities to reproduce tensile tests at low and medium strain rates. However in both cases, models were developed and validated for polymers only in their glassy state. Rare are the models that are capturing polymers behaviour from their glassy to near the liquid state of the material.

In front of these drawbacks, Billon et al. [1], [2] proposed to combine the hyperelastic model of Edward and Vilgis [32], which accounts for the density of entanglements and crosslinks, with the evolution of internal state variables (ISVs) to incorporate inelastic mechanisms. In this attempt, good results were obtained for capturing the response of PMMA and PA66 under non-monotonic loadings. However, the initial “rigidity” of the material was underestimated. Then, Gehring et al. [33] proposed to enrich the model by adding additional processes to account for the effect of secondary bonds. Despite satisfactory results on PET, the accuracy of the model was tested just at moderate strain levels, around 30%. Therefore, the domain of large deformations is still unexplored. Additionally, the use of the “equivalent strain rate at reference temperature”, which have proven to be efficient from an experimental point of view [34], is still not totally included in this way of modelling. In addition, this model has not yet been validated for a wide range of conditions, corresponding to near-liquid, rubbery state, viscoelastic and near glassy states. Moreover, another key issue could be to understand how the internal state variables (such as the entanglements or weak bond interactions) depend on molar mass and crosslinking degree.

In this work, we aim at validating the versatility of the model proposed by Billon et al. [1], [2] and extended by Gehring et al. [33]. Thus, the purpose of this present effort is to extend the model validation by exploring its capabilities to capture non-monotonic tensile loadings at large deformation for a high number of experimental conditions, while accounting for the concept of equivalent strain rate for PMMAs of different molecular weights and crosslinking degree.

This paper proceeds first by a mechanical characterization of PMMAs with different molar masses in low and large deformation domains. Both dynamic mechanical thermal analysis experiments and uni-axial tensile tests coupled with digital image correlation are performed over a wide range of temperatures and strain rates under non-monotonic loading. Then, the formalism of the model, proposed by Billon [1] and Gehring et al. [33], is described. Following, a comparison between experimental results and constitutive modelling is presented. Finally, constitutive parameters are discussed.

2 Materials and methods

2.1 Materials

ALTUGLAS® PMMAs of different molar masses and supplied by Arkema Company were used. Depending on mass they were available either as injection molded, extruded or casted 3-mm thick plaques. All samples were tooled to dimensions suitable for given experimental technics with special attention to avoid any heating. Table 1 summarizes the physical properties of the materials: weight average molar mass, *Mw*, number average molar mass, *Mn*, density at room temperature, ρ, α transition temperature at 1 Hz, T_α (or glass transition temperature determined from DMA tests performed at a heating rate of 1°C/min), glass transition temperature, Tg, as measured by differential calorimetric analyses (DSC), and processing technics. The calorimetric analyses were carried out in a DSC Perkin Elmer 8500®, calibrated with indium. All the DSC tests were realized in a nitrogen atmosphere at a heating rate of 10°C/min from room temperature up to 160°C. Materials did not exhibit any relevant optical nor mechanical anisotropy, so orientation of molecules was assumed to be negligible. As all data were gathered above glass transition temperature, aging effects did not have to be accounted for, i.e. PMMAS were renewed by pre-heating. Experiments were then performed without any additional annealing or conditioning. For clarity in the following, the PMMAs are referred by using their molar mass in weight.

Table 1: Material Properties

Processing	***Ref.***	ρ **(g/cm^3)**	T_α ***at 1Hz(°C)***	***Tg (°C)***	M_w **(Kg/mol)**	M_n **(Kg/mol)**
Injection molding	PMMA 80	1.18	108	108	80	42

Extrusion	PMMA 120	1.19	120	113	120	62
Casting molding	PMMA 3500	1.20	132	119	3500	880
Casting molding	PMMA CL	1.20	133	122	Cross-linked Copolymer	

2.2 Tensile testing

Mechanical response at large deformation was addressed using loading-unloading tensile tests performed on an Instron 596 electro-mechanical load frame with a thermal chamber. To make strain rate as constant as possible during test, machine was driven through an exponential ramp. The samples geometry was a home designed dog bone shape (see Fig. 1 a)). Design was made for the strain field in the process zone to remain homogeneous and strictly uniaxial. Such homogeneity was verified through the use of Digital Image Correlation (DIC) during tension. Two cameras in stereo-correlation were used (Fig. 1 b)) for measuring the strain fields using digital image correlation [35], [36] on painted random speckle patterns. Those latter were obtained by spraying black and white paints. Stereo-correlation enabled addressing the 2D strain field on the face of the samples accounting properly for out of plane displacements (parallel to thickness). DIC was carried out using VIC-3D® software. An example of the true longitudinal strain field is presented in Fig. 1 c) for a tensile test performed at 130 °C and $1.5x10^{-2}$ s^{-1} on PMMA 80. To obtain accurate results, a mesh sensitivity study was performed [34], [37]–[40], concluding that a subset size of 21 by 21 pixels, a step size of 2 pixels and a filter size of 15 were appropriated for the correlation.

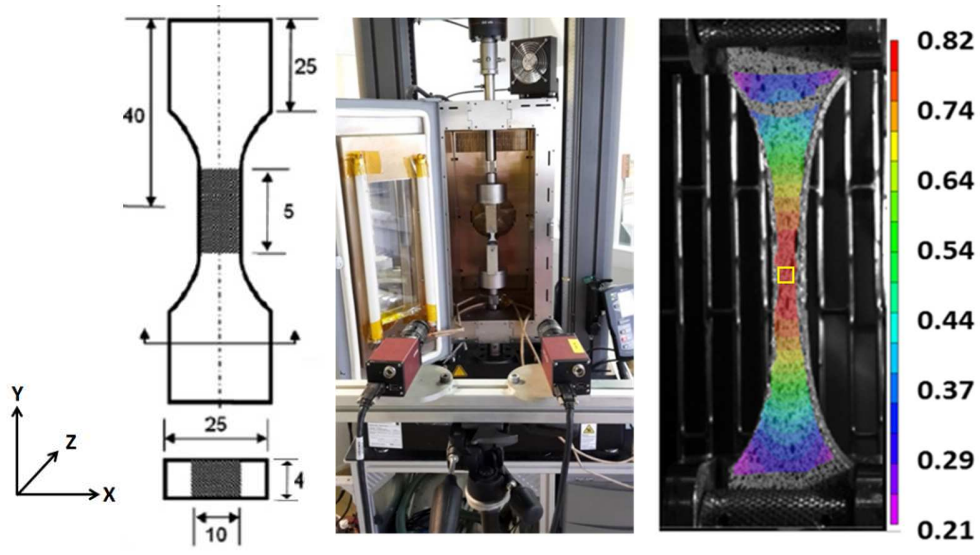

a) b) c)

Fig. 1: a) Geometry of tensile sample. b) Experimental set-up displaying the mechanical testing machine with a thermal chamber, stereovision system and lightening. c) Iso-longitudinal Hencky's strain maps of PMMA 80 stretched at 130 °C and $1.5x10^{-2}$ s^{-1}.

The local constant true strain rates ranged from 10^{-3} s^{-1} to 10^{-2} s^{-1}. All the tests were performed by loading the material up to a local true strain of 80% and then unloading to zero forces at the same constant local strain rate. The data used to generate the true stress-true strain curves, i.e. longitudinal, ε_{yy} and transversal, ε_{xx}, Hencky's strains, was obtained from the information within the central zone of the samples where deformation was homogeneous, as indicated in Fig. 1c). Assuming transverse isotropy (i.e., strain in the Z- direction equal to strain in the X- direction) [41], [42], the true stress could then be expressed as:

$$\sigma_T = \frac{F}{A_{(t)}} = \frac{F}{A_0 exp(2\varepsilon_{xx})} \quad (1)$$

where $A_{(t)}$ and A_0 are the local cross section and the initial local cross section of the sample in the measuring area, respectively.

Such assumption was validated by observing the local deformation from the specimen front and thickness.

All the samples were pre-heated during ten minutes for ensuring a homogeneous temperature (ranging from 100 °C up to 200 °C).

2.3 Experimental database

It was previously demonstrated that dependences of mechanical behaviour of PMMA upon temperature and strain rate can be merged in the dependence upon one unique parameter, i.e. the equivalent strain rate at a reference temperature issued from classical time temperature superposition principle. This approach was successfully applied for various polymers [2], including PMMA [34], [43]. Usual William-Landel-Ferry, WLF, equation [44] was used.

According to that approach any testing, characterised by the set of conditions: (testing temperature, T_1, strain rate during loading and unloading,$\dot{\varepsilon}_1$), is mechanically equivalent to all other conditions, (T_k, $\dot{\varepsilon}_k$) such as (Eq.(2):

$$a_{T_1/T_0}\dot{\varepsilon}_1 = a_{T_k/T_0}\dot{\varepsilon}_k = \dot{\varepsilon}_{eq} \quad (2)$$

where $\dot{\varepsilon}_{eq}$is the *equivalent strain rate at reference temperature*. T_0 and $a_{T/T0}$ are the reference temperature and the so-called shift factor whose more usual form is the WLF one (Eq. (3)):

$$a_{T_j/T_0} = 10^{\frac{-C_1(T_j - T_o)}{C_2 + T_j - T_o}} \quad (3)$$

In this study, a common-to all PMMAs reference temperature of 130 °C was chosen that remained close to glass transition temperature of any materials. Time-temperature superposition principle was addressed through dynamic mechanical thermal analysis (DMTA) by frequency at various isotherms (more information is given in [34]). Master curves of viscoelastic propoerties were built, obtining different C_1 and C_2 parameters that are gathered in Table 2.

Table 2: WLF parameters, To = 130 °C

Coefficient	*PMMA 80*	*PMMA 120*	*PMMA 3500*	*PMMA CL*
C_1	4.5	6.5	8.8	11.5
C_2 (°C)	66.3	64.7	68.1	79.2

Efficiency of the equivalent strain rate approach was illustrated in [34]. Relation between technological conditions and equivalent strain rate are summarised in Table 3. As displayed in Figs. 8 to 11, it is clear that, depending on loading conditions and molar mass, mechanical behaviour of PMMA can appear to be elasto-viscoplatic, visco-elastic or even hyperelastic body. Obviously, modelling those large evolutions using one model is a challenge. This is the topic this paper deals with.

Table 3: Temperature and strain rate pairs for obtaining the same equivalent strain rate at a reference temperature of 130°C.

	Equivalent Strain Rate (s^{-1})					
PMMA	10^{-8}	10^{-6}	10^{-4}	10^{-2}	10^{0}	10^{2}
80	-	-	-	130°C/0.017s^{-1} 119°C/0.002s^{-1}	110°C/0.017s^{-1} 103°C/0.002s^{-1}	97°C/0.017s^{-1} 93°C/0.002s^{-1}
120	-	-	157°C/0.017s^{-1} 140°C/0.002s^{-1}	130°C/0.017s^{-1} 120°C/0.002s^{-1}	115°C/0.018s^{-1} 107°C/0.002s^{-1}	106°C/0.020s^{-1} 101°C/0.002s^{-1}
3500	196°C/0.019s^{-1} 185°C/0.002s^{-1}	177°C/0.018s^{-1} 170°C/0.002s^{-1}	150°C/0.017s^{-1} 140°C/0.002s^{-1}	130°C/0.019s^{-1} 124°C/0.002s^{-1}	118°C/0.019s^{-1} 114°C/0.002s^{-1}	109°C/0.021s^{-1} 107°C/0.002s^{-1}
CL	-	173°C/0.016s^{-1} 160°C/0.002s^{-1}	147°C/0.016s^{-1} 138°C/0.002s^{-1}	130°C/0.016s^{-1} 122°C/0.002s^{-1}	118°C/0.017s^{-1} 113°C/0.002s^{-1}	109°C/0.026s^{-1} 106°C/0.002s^{-1}

3 Theoretical

The model used in this paper was inspired by studies on the viscohyperelastic nature of polymers above *Tg* [1] [46]. This model was written in 3D form in the frame of thermodynamics [2]. Further improvements were then suggested to offer a better fitting of initial rigidity of PET [33] .

Main interest of this model is its ability reproducing visco-elastic loops (loading-unloading) using only a few parameters. Second interest is that it relies on concepts from polymer physics, which is expected to help drawing of relationships with polymers structure.

Following this model, the behaviour of the polymer is considered to be equivalent to that of a homogeneous equivalent statistical network of chains of limited extensibility (that provides hyperelasticity), constrained by entanglements and crosslinks. Such network may experience

inelasticity when deformed. Those changes should result in gain or loss of extensibility of active chains or in the nature of the entanglements.

For accounting all these factors, Billon [1] suggested to use the non-Gaussian hyperelastic strain energy function, ψ, proposed by Edward and Vilgis (EV) [32]. The function considers that the storage energy in the polymer network is associated to the entanglements and the crosslinks. Other authors [18]–[21], [47]–[51], have used the Edward and Vilgis' strain energy to reproduce the mechanical response under tensile and compression loadings for amorphous and semi-crystalline polymers in a more usual manner, i.e. as an element in analogical models.

The inelastic part of the strain rate is ruled by the energy balance to compensate the changes in energy induced by the evolution of the microstructure and/or changes of the topology when the material is deformed. Last works [33] suggested that elasticity and hyperelasticity in amorphous polymers come from changes in entropic conformational energy enables by three main topological factors: entanglements, crosslinks and weak bonds (van der Waals, hydrogen bonds).

Mechanical effects sensitive to entanglements and crosslinks, on one hand, and to weak bonds, on the other hand, are set into two parallel revisited Edward and Vilgis [32] networks (branches 1 and 2 as displayed in Fig. 2).

Strain energy is ruled by Edward Vilgis' potential in each branch. The initial equation was reported in the literature as a function of the principal stretch ratios but can easily be rewritten as a function of the stretch ratio tensor invariants (Eq. (4)).

$$\psi^i\begin{pmatrix} I_1^i, I_2^i, I_{3,}^i \\ N_c^i, N_s^i, \\ \eta^i, \alpha^i \end{pmatrix} = \frac{1}{2}k\theta\left[\begin{array}{c} N_c^i\left(\frac{\left(1-{\alpha^i}^2\right)I_1^i}{1-{\alpha^i}^2 I_1^i} + ln\left(1-{\alpha^i}^2 I_1^i\right)\right) + \\ N_s^i\left(\frac{\left(1+\eta^i\right)\left(1-{\alpha^i}^2\right)\left(I_1^i + 2\eta^i\, I_2^i + 3{\eta^i}\, I_3^i\right) I_1^i}{\left(1-{\alpha^i}^2\, I_1^i\right)\left(1+\eta^i\, I_1^i + {\eta^i}^2\, I_2^i + {\eta^i}^3\, I_3^i\right)} + \right. \\ \left. ln\left(\left(1-{\alpha^i}^2\, I_1^i\right)\left(1+\eta^i\, I_1^i + {\eta^i}^2\, I_2^i + {\eta^i}^3\, I_3^i\right)\right)\right) \end{array}\right] \quad (4)$$

In Eq. (4) index *i* refers to the given branch (1 or 2). $I_1^i, I_2^i\ and\ I_3^i$ are the invariants of the elastic stretch ratio tensor in branch *i*. κ is the Boltzmann's constant and θ is the absolute temperature. N_c^i is the number of crosslinks per unit volume in branch *i*. N_s^i is the number of entanglements per unit volume in branch *i*. α^i is the chain extensibility factor (being 0 in the case of a Gaussian chain) and η^i is related to the degree of mobility of the entanglements. A zero η-value corresponds to a permanent node (crosslink).

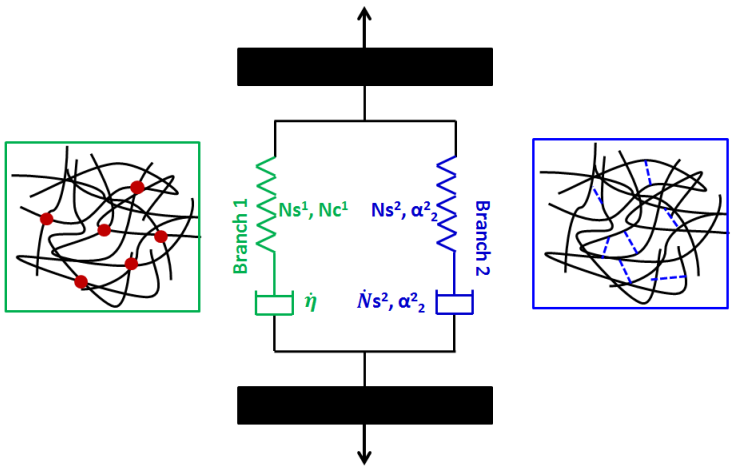

Fig. 2: Schematic representation of topological interactions responsible for microstructural changes when the polymer is deformed. Red dots correspond to crosslinks and dotted blue lines represent weak interactions.

To study the model capabilities, we will restrain our study to the description of tensile loading in 1D assuming incompressibility. Due to incompressibility I_3^i are equal to 1. The Cauchy stress for uniaxial loading is then defined in branch *i* as Eq. 5

$$\begin{cases} \sigma^i = 2\left({\lambda_e^i}^2 - \dfrac{1}{\lambda_e^i}\right)\left(\dfrac{\partial \psi^i}{\partial \mathrm{I}_1^i} + \dfrac{1}{\lambda_e^i}\dfrac{\partial \psi^i}{\partial I_2^i}\right) \\ \mathrm{I}_1^i = \dfrac{2}{\lambda_e^i} + {\lambda_e^i}^2 \\ \mathrm{I}_2^i = \dfrac{1}{{\lambda_e^i}^2} + 2\,\lambda_e^i \end{cases} \tag{5}$$

where λ_e^i is the elastic part of the stretch ratio.

We assume a multiplicative decomposition of stretch ratio, λ_e^i, λ_v^i in any branch. In consequence stretch ratio in branch λ^i is given in Eq. (6).

$$\lambda^i = \lambda_e^i \lambda_v^i \tag{6}$$

According to the model [1, 33] at any time, *t*, and in any branch *i*, inelastic strain rate is deduced from energy releases related to the evolutions of some internal variables characterising the network. 1D form of the concept is reminded in Eq. (7). More precisions for 3D writing are given in ref [33].

$$\frac{d\varepsilon_v^i}{dt} = \frac{1}{\sigma^i}\left(\frac{\partial \psi^i}{\partial \eta^i}\frac{d\eta^i}{dt} + \frac{\partial \psi^i}{\partial N_s^i}\frac{dN_s^i}{dt} + \frac{\partial \psi^i}{\partial {\alpha^i}^2}\frac{d{\alpha^i}^2}{dt}\right) \; with \; \frac{d\lambda_v^i}{dt} = \frac{d\varepsilon_v^i}{dt}\lambda_v^i \tag{7}$$

Branch 1 experiences a decrease in η^1 parameters keeping other constant. This represents the effect of potential disentanglements under loading. Branch 2 experiences changes in the weak bonds between chains (van der walls bonds for example) that disappear under loading and are restored upon unloading. The evolution of the chains arrangements or microstructure with the deformation depends on the elastic energy stored in the equivalent network. Therefore, stored energy is the driving force to describe the kinematic of the evolution of the internal state variables, which controls inelastic strain rate in each branch. To quantify the elastic stored energy, we define $\Delta\psi^i$as the difference between the energy of the deformed polymer and the initial energy (Eq. (8)).

$$\Delta\psi^i = \psi^i \begin{pmatrix} I_1^i, I_2^i, I_{3,}^i \\ N_c^i, N_{s,}^i \\ \eta^i, \alpha^i \end{pmatrix} - \psi^i \begin{pmatrix} 3,3,1, \\ N_c^{i,0}, N_s^{i,0}, \\ \eta^{i,0}, \alpha^{i,0} \end{pmatrix} \tag{8}$$

where $N_c^{i,0}, N_s^{i,0}, \eta^{i,0}\ and\ \alpha^{i,0}$ are initial values for $N_c^i, N_s^i, \eta^i\ and\ \alpha^i$, respectively.

Increase in chain slippage freedom occurs only in branch 1 when the polymer is deformed. Indeed, an increase of this variable can be related to the disentanglement of the polymer chains when an external load is applied. The evolution kinetics is assumed to follow the next forms (Eq. (9)):

$$\frac{d\eta^1}{dt} = Z\ \Delta\psi^{ip1} \tag{9}$$

where *Z* and *p* are material parameters. In Branch 1, the parameter η was chosen to evolve from the arbitrary initial value $\eta^{1,0} = 0.2343$ as proposed elsewhere [32], [51]. In parallel, weak bonds branch was assumed that:

$$\frac{d\eta^2}{dt} = 0;\ \eta^{2,0} = 0 \tag{10}$$

Density of entanglement does not vary in branch 1 and as we only consider isothermal tests, let's define N_{s1} as (Eq. (11)):

$$N_{s1} = k\theta N_s^1 = k\theta N_s^{1,0} \tag{11}$$

In the same manner, one defines $N_{s2} = k\theta N_s^2$ but this weak bond density decreases when the polymer is deformed. As proposed by Gehring et al. [33], we will state that an equilibrium value exists (N_s^{lim}) which depends on the amount of available energy. Therefore, the rate of decrease or increase is assumed to be proportional to the gap between the instantaneous density of bonds and that limit. We will also consider that the rate of decrease is different from the rate of increase. Equation (12) summarises those choice.

$$\begin{cases} N_s^{lim} = \dfrac{N_{s2}^0}{1+(\tau_s \Delta\psi^2)^{\xi}} \\ N_s^{lim} - Ns_2 > 0 \;\; then \; \dfrac{dN_{s2}}{dt} = v\left|N_s^{lim} - Ns_2\right|^2 \\ N_s^{lim} - Ns_2 \leq 0 \;\; then \; \dfrac{dN_{s2}}{dt} = -v'\left|N_s^{lim} - Ns_2\right|^2 \end{cases} \quad (12)$$

where N_{s2}^0, v, v', ξ, p are material parameters. N_{s2} is, for its part, the density of weak links at a given time, being N_{s2}^0 the initial value.

For high levels of deformation, polymer chains are fully stretched and cannot longer be extended. This is defined by the chain extensibility. This variable will depend on the number of chain interactions that will act as junction points. For convenience, we consider the topological constrain that will affect the extensibility as the number of weak bonds (Branch 2) [33]. Thus, following initial definition for those parameters [32] we assume that the kinetics of evolution α^{2^2} is proportional to Ns_2 which leads to Equation (13):

$$\begin{cases} \dfrac{d\left(\alpha^{2^2}\right)}{dt} = \dfrac{\alpha^{2,0^2}}{N_{s2}^0}\dfrac{dN_{s2}}{dt} \\ \dfrac{d\left(\alpha^{1^2}\right)}{dt} = 0 \end{cases} \quad (13)$$

Last choice is to consider that, in branch 1, chains are totally extensible, meaning $\alpha^{1^2} = 0$.

Inverse analysis method was used to identify the optimal set of parameters for describing the experimental results test by test. The study was carried out by using least squares method and using the simplex algorithm of the "fminsearch" MATLAB® function, which uses the Nelder-Mead simplex algorithm [52] as described in Lagarias et al. [53].

4 Results and Discussions

4.1 Parameters and internal state variables

To analyse the capability of the model to reproduce important mechanical features regarding material response from quasi-viscous fluids up to glassy solids, the entire data base was fitted. The identified sets of parameters (estimated test by test) for PMMAs are showed in Table A1.1 and Table A1.2 of Annex 1.

Fig. 3 depicted those parameters as a function of equivalent strain rate at 130 °C, compared to evolution of storage modulus (*E'*) and loss modulus (*E''*) master curves obtained during DMTA analysis with a reference temperature of 130 °C. For those latter, abscissa consist in strain rate

estimated from frequency, *f*, [44] accounting for the fact that maximum strain was 0.001 during the tests ($\dot{\varepsilon} = 4.f.0.001$).

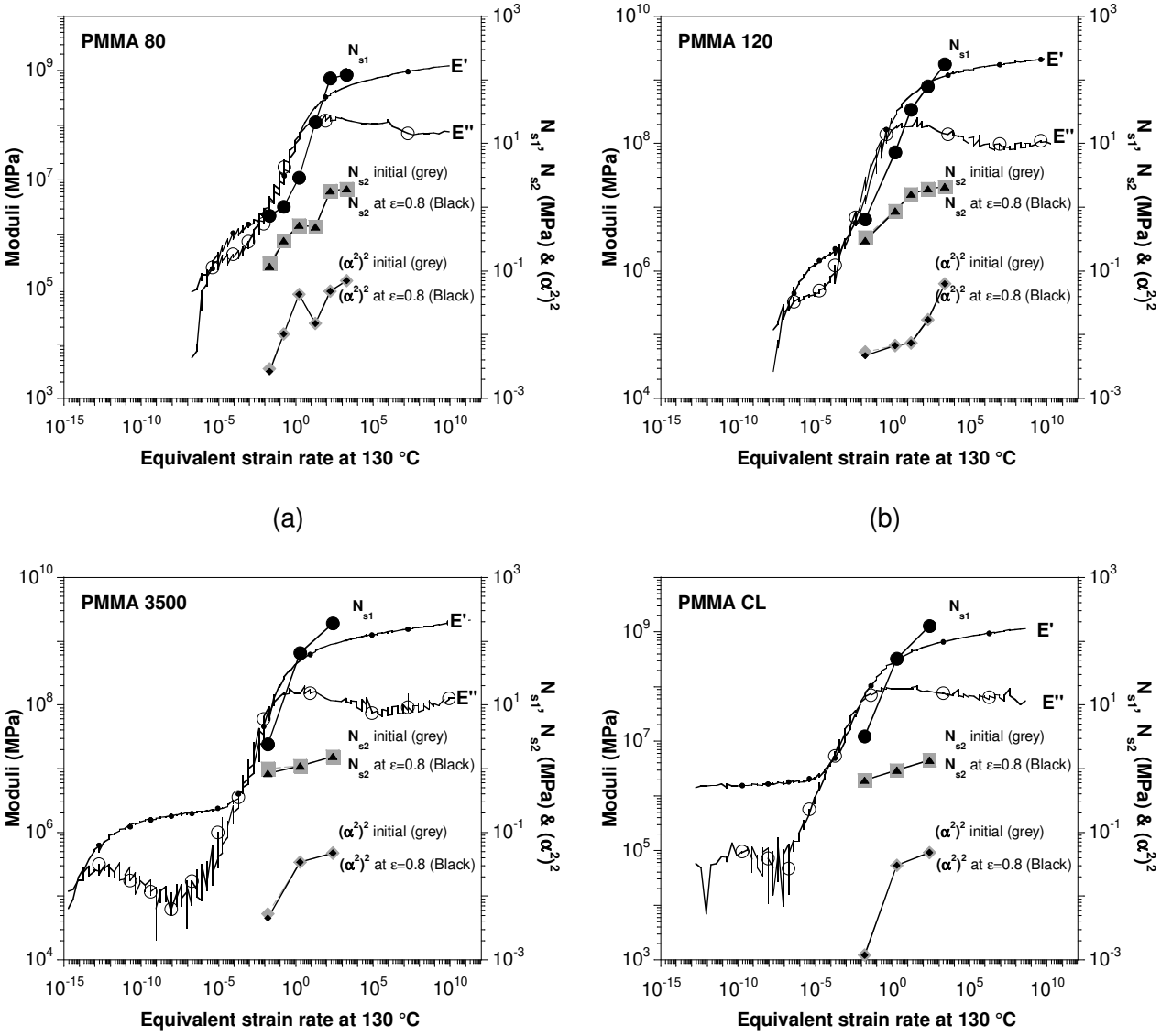

Fig. 3: Parameters of the model vs. equivalent strain rate at 130 °C. Comparison with DMTA results for: a) PMMA 80; b) PMMA 120; c) PMMA 3500; d) PMMA CL.

First observation is that N_{s1}, N_{s2} and $(\alpha^2)^2$ increase with increasing strain rate in an equivalent manner than *E'* and *E''* do. N_{s2} and $(\alpha^2)^2$ decrease slightly during loading for any strain rate. This is illustrated in Fig. 3 by plotting their values for a strain of 0.8 compared to initial values. One can observe that, in our case, these decreasing are low (10% to 15% at low strain rate in the rubbery plateau). However, this can be enough to induce some visco-elastic effects above *Tg*. The relative importance of active entanglements and active weak bonds depends on the strain rate. Indeed, N_{s2} is

significantly lower than N_{s1} in the glassy state and has the same order of magnitude in the rubbery state. This implies that relative importance of branch 1 and 2 depends on strain rate.

The η^1 parameter, for its part, increases more significantly close to rubbery state (e.g. low strain rate or high temperature) (see for example Fig. 4). Rate of evolution is low in the initial regime of loading and then increases up to a limiting value (Fig. 5). This limit is higher in the rubbery state for PMMA 80 and 120 but lower for PMMA 3500 and CL.

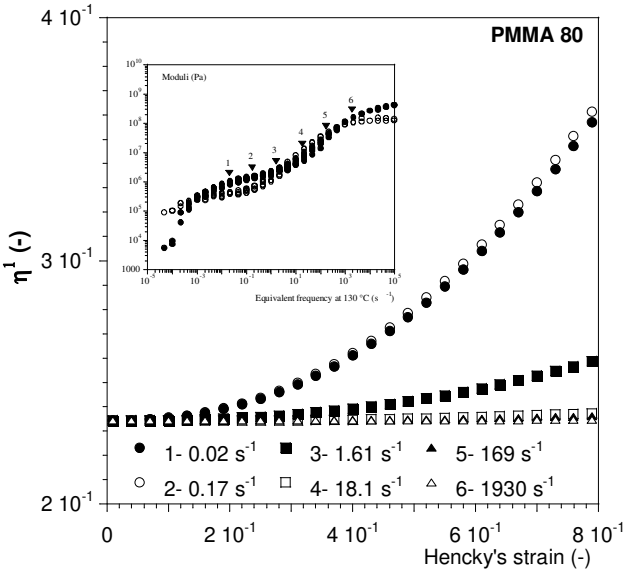

Fig. 4: η^1 vs. Hencky's strain during tension at different strain rates for PMMA 80.

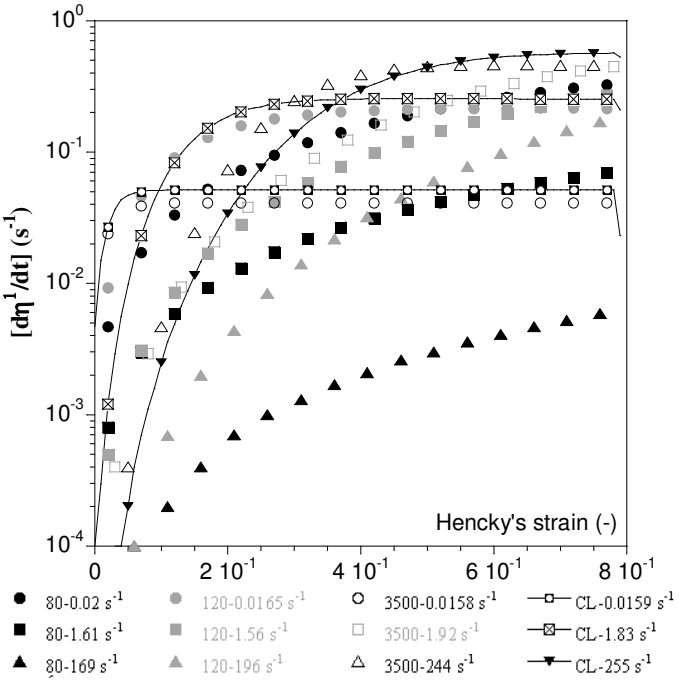

Fig. 5: Rate of change of η^1 vs. Hencky's strain during tension at different strain rates for PMMA 80, 120, 3500 and CL.

In consequence, evolution of η parameter can be diverse depending on PMMAs. It increases from rubbery to glassy states for PMMA 3500 and CL, in a quite equivalent manner. It decreases for PMMA 80 and 120.

However, that apparent contradiction disappears when focusing on rate of energy dissipation ($N_{s1}\, d\eta^1/dt$) on Fig. 6. Rate of energy dissipation is always higher at higher strain rate (glassy region) and increases with the molar mass. Once again PMMA CL is equivalent to PMMA 3500.

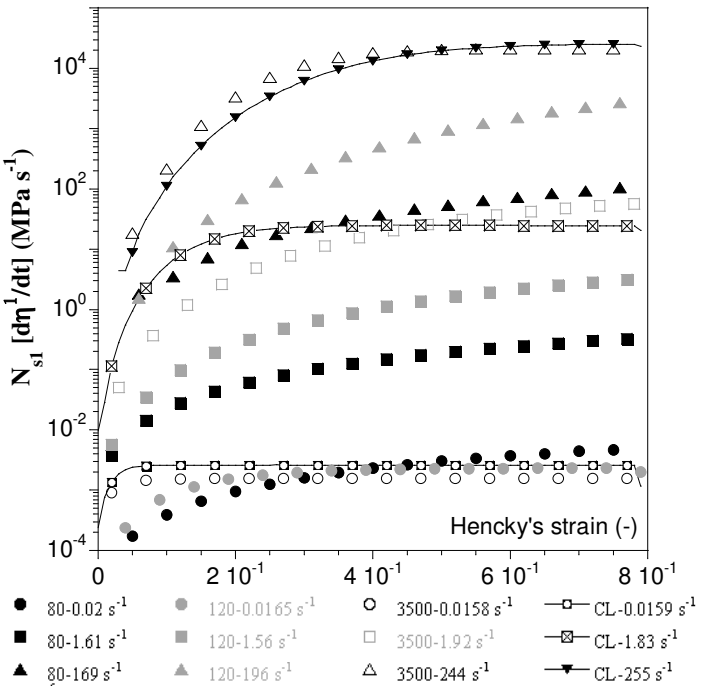

Fig. 6: Rate of energy dissipation in branch 1 vs. Hencky's strain during tension at different strain rates for PMMA 80, 120, 3500 and CL.

In conclusion, *close to the glassy* state equivalent network initially consists mainly in mobile entanglements whose mobility increases upon loading. The number of entanglements slightly depends on molar mass, being more numerous for high molar mass. Anyway, part of the difference between our PMMAs from "entanglements point of view" appears to be their ability to gain mobility upon stretching. The increase in mobility is faster at low strain rate for low molar mass PMMAs but slower for high molar mass. At this point, one can argue that the model would need some enrichment to account for the complexity of combining the tightness of entanglement, their lifetime and their restoration kinetics. The model displays a good compromise between entanglements number and mobility gain. In any case, inelasticity is due to those effects. Weak bonds, less numerous than entanglements, acts as "permanent" nodes, seemingly due to a too long life time compare to loading speed in that region. Closer to rubbery state, entanglements and weak bonds co-exist in equivalent densities. Entanglements gain mobility rapidly so that they should not be active for long.

4.2 Relevance of the model

4.2.1 Linear domain

Parameters identified for each PMMA were used to compute the apparent Young's modulus, *E*, by using the EV's energy as (calculation in Annex 2):

$$E = 3kT\left[\begin{array}{c}\dfrac{N_s^i\left\{\left(1-\alpha^{i^2}-2\eta^i\alpha^{i^2}\right)\left(1-3\alpha^{i^2}\right)+2\alpha^{i^2}\left(1+\eta^i\right)^2\right\}}{(1+\eta^i)^2(1-3\alpha_k^2)^2} \\ + \\ \dfrac{N_c^i\left\{\left(1-\alpha^{i^2}\right)\left(1-3\alpha^{i^2}\right)+2\alpha^{i^2}\right\}}{\left(1-3\alpha^{i^2}\right)^2}\end{array}\right], i=[1,2] \quad (14)$$

Then, we compared this modulus with the master curves of the storage modulus presented in section 2.3. This is depicted in Fig. 7 for PMMA 120 and PMMA CL, respectively. Experimental results are in good agreement with those obtained through equation (14). Moreover, we can notice that Young's modulus determined from Branch 1, *E1*, exhibits a bigger contribution to the total stiffness than the one of Branch 2. Therefore, the model displays a good reliability not just at large strain but also in the linear domain of deformation.

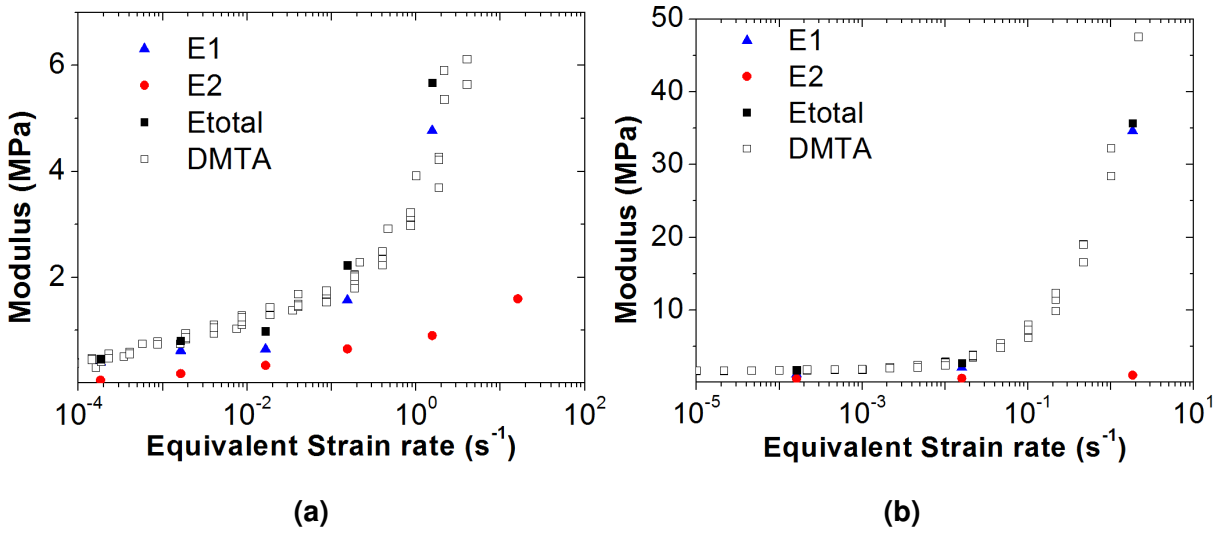

Fig. 7: Comparison between elastic modulus determined from DMTA tests and those identified through EV's strain energy function: a) PMMA 120, b) PMMA CL.

4.2.2 Large deformation

The comparison between the experimental (dots) and model (lines) stress-strain curves is presented in Figs. 8 - 11 for the identified set of parameters for PMMAs displayed in Annex 1. Results suggest that the model used in this work has enough degrees of freedom to reproduce the experimental tensile curves with a good agreement using ten parameters per condition. Indeed, the model has the potential

to capture the different features of the mechanical curves during loading to large strain levels (between 80% and 100%) and also during the unloading. Within our base of experimental conditions, mechanical response of the PMMAs ranges from quasi-viscous fluids up to glassy solids for PMMA 80 and 120 from a rubbery-like state (10^{-6} s^{-1}) to a more glassy state (10^{0} s^{-1}) for PMMA 3500 and CL. Regardless such strong difference, the model was able to reproduce all these conditions, proving its adaptability and efficiency.

However, to be complete near the glassy region (10^{2} s^{-1}), the model showed to be less efficient, especially for PMMA 3500. For this condition, the apparent elastic regime was slightly underestimated and the apparent yield point and softening were not captured by the model. Nevertheless, at higher strains (above 20%), the behaviour in the plastic region and the strain hardening were well described, as well as the unloading. For future works, it can be suggested to include a kinetic form of the density of entanglements on Branch 1. This could account for a decrease with deformation, which could enhance the description of the softening.

Overall, we can conclude that the constitutive model used in this work presents a good accuracy when the material is tested under non-monotonic tensile loading up to large deformation level near the flowing region, in the rubbery state and in its viscoelastic region, but may lead to more discrepancies when the material is near the glassy region.

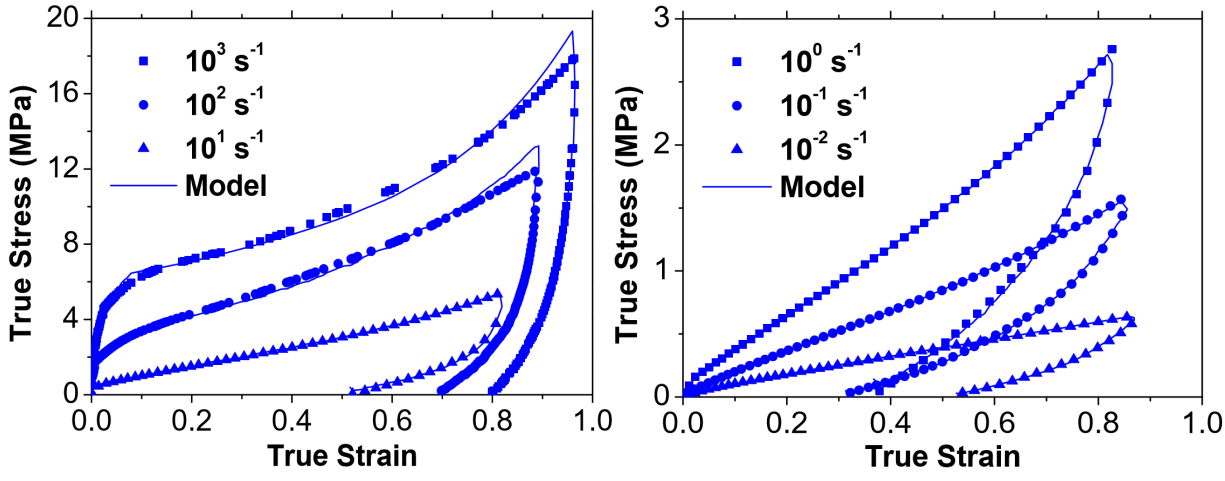

Fig. 8: Comparison between experiments (dots) and model (lines) on load-unload tensile tests on PMMA 80 at $\dot{\varepsilon}_{eq}$ at 130 °C: a) 10^{3} s^{-1}, 10^{2} s^{-1}, 10^{1} s^{-1} and b) 10^{0} s^{-1}, 10^{-1} s^{-1}, 10^{-2} s^{-1}. (please refer to Table 3 for the related temperature and strain rate used for these tests)

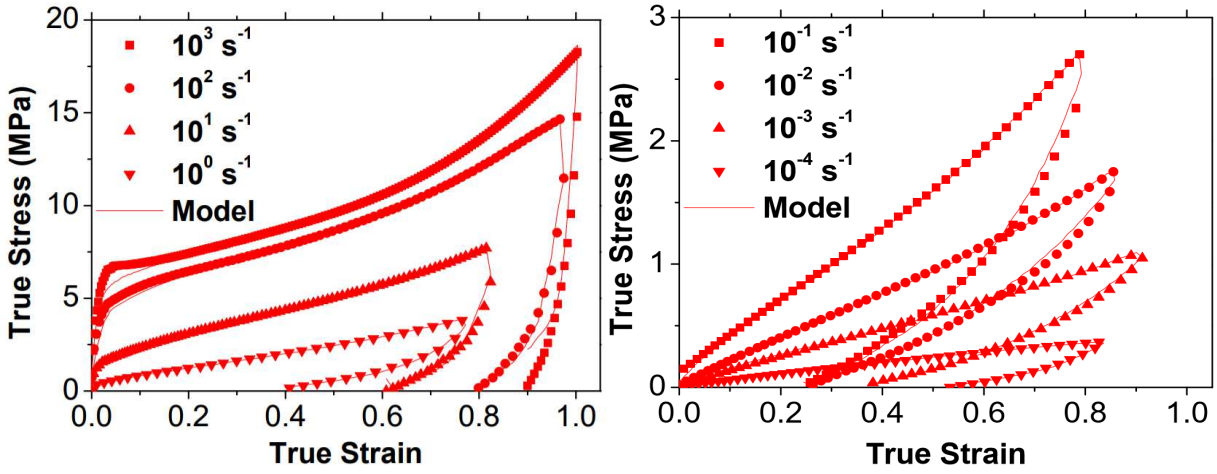

a)

b)

Fig. 9: Comparison between experiments (dots) and model (lines) on load-unload tensile tests on PMMA 120 at $\dot{\varepsilon}_{eq}$ at 130 °C: a) 10^3 s^{-1}, 10^2 s^{-1}, 10 s^{-1}, 10^0 s^{-1} and b) 10^{-1} s^{-1}, 10^{-2} s^{-1}, 10^{-3} s^{-1}, 10^{-4} s^{-1}. (please refer to Table 3 for the related temperature and strain rate used for these tests)

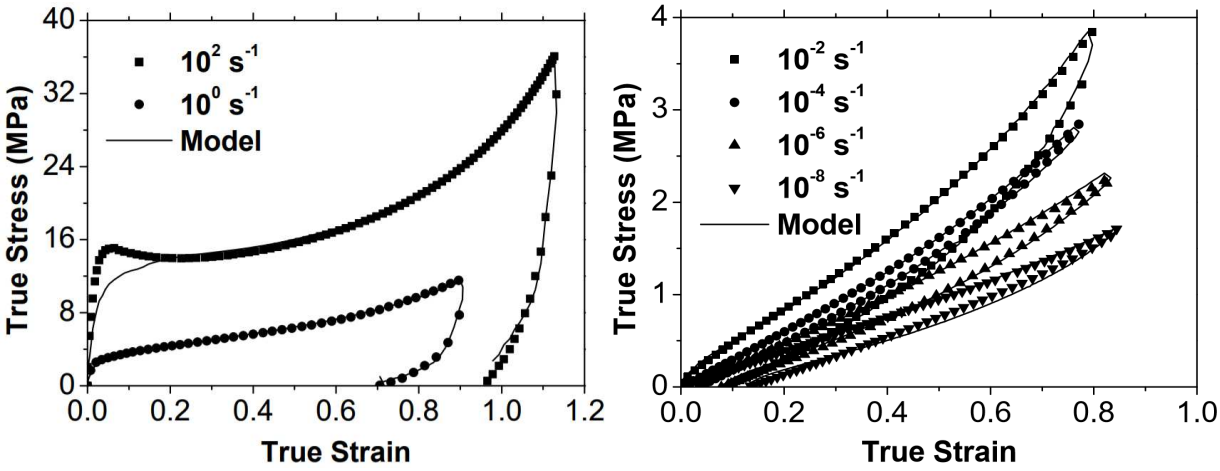

a)

b)

Fig. 10: Comparison between experiments (squares) and model (lines) on load-unload tensile tests on PMMA 3500 at $\dot{\varepsilon}_{eq}$ at 130 °C: a) 10^2 s^{-1}, $10^0 s^{-1}$ and b) 10^{-2} s^{-1}, 10^{-4} s^{-1}, 10^{-6} s^{-1}, 10^{-8} s^{-1}. (please refer to Table 3 for the related temperature and strain rate used for these tests)

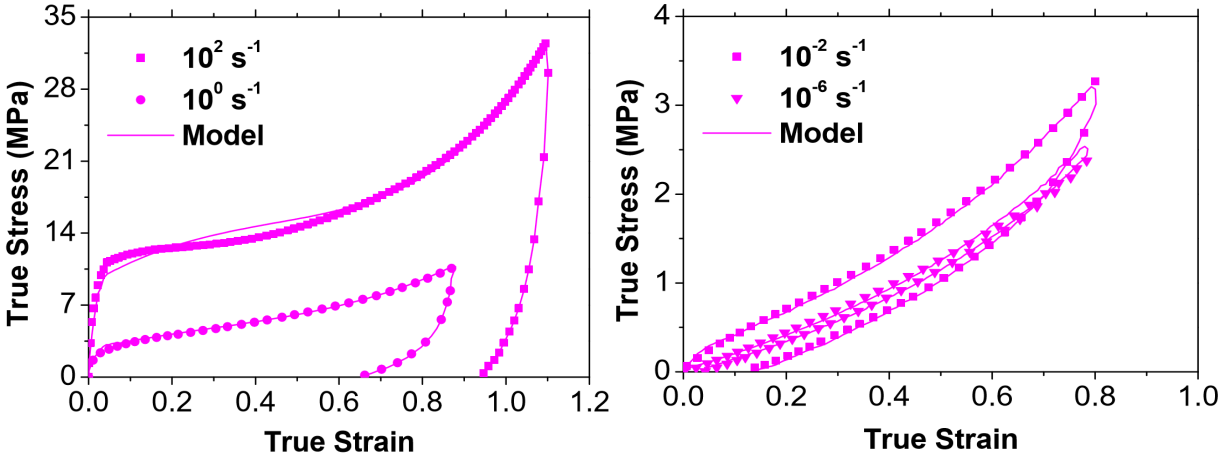

Fig. 11: Comparison between experiments (squares) and model (lines) on load-unload tensile tests on PMMA CL at $\dot{\varepsilon}_{eq}$ at 130 °C: a) 10^2 s^{-1}, 10^0 s^{-1} and b) 10^{-2} s^{-1}, 10^{-4} s^{-1}. (please refer to Table 3 for the related temperature and strain rate used for these tests)

4.3 Contribution of each branch on the overall mechanical response

In this section, we aim at illustrating the contribution of each branch, i.e; entanglements and weak bonds contributions, to the global mechanical response at equivalent strain rates below and above the α-transition.

4.3.1 Below α-transition

Fig. 12 shows the contribution of each branch to the total stress for PMMA 120 for an equivalent strain rate of 10^3 s^{-1}. This condition corresponds to the glassy region of this PMMA. Branch 1 describes the initial regime, often named “elastic” regime, and contributes to most of the mechanical stiffness up to a strain of 80%. Additionally, this branch also accounts for most of the energy dissipation. This branch describes an elastoviscoplastic-like material. Branch 2 contributes to the nonlinear strain hardening, which becomes more noticeable above a strain of 80%. Moreover, Branch 2 displays almost no hysteresis. This branch accounts for the hyperelastic response of the material. Notice that these trends were observed for all PMMAs.

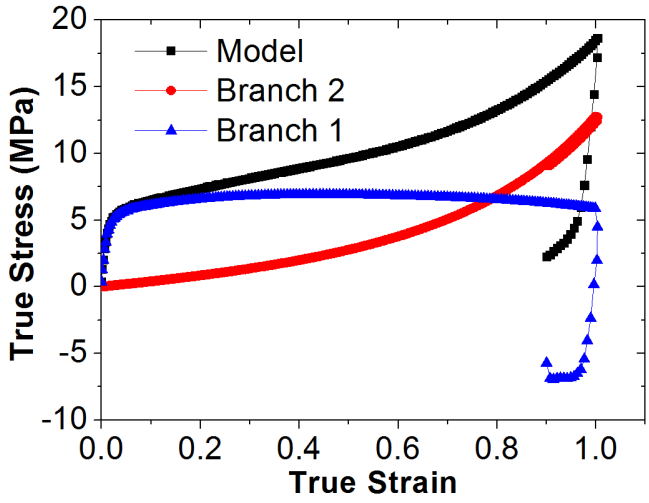

Fig. 12: Contribution of each branch to the total stress-strain curves for PMMA 120 at 130 °C for an equivalent strain rate of 10^3 s^{-1}. (please refer to Table 3 for the related temperature and strain rate)

4.3.2 Viscoelastic region

Fig. 13 displays the contribution of each branch to the total stress for PMMA 120 for an equivalent strain rate of 10^0 s^{-1}. This condition corresponds to the viscoelastic region of this PMMA 120. Branch 1 still captures most of the initial regime but its contribution to the mechanical stiffness is less significant above 20% of deformation. Additionally, energy dissipation is lower than in the glassy region. Thus, this branch acts as a viscoplastic-like body. Branch 2 represents the main source of strain hardening at large deformation (above 20%). Regarding its contribution to inelasticity, we can see that energy dissipation is slightly higher than in the glassy region. Therefore, Branch 2 acts now as a viscohyperelastic network. Same conclusions were drawn for all PMMAs.

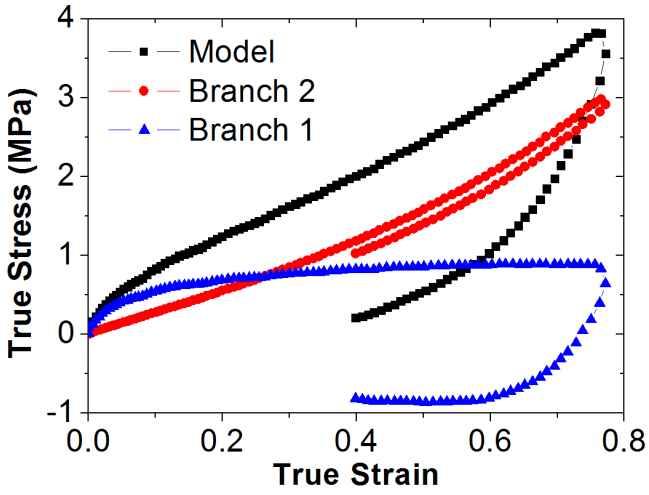

Fig. 13: Contribution of each branch to the total stress-strain curves for PMMA 120 at 130 °C for an equivalent strain rate of 10^0 s^{-1}. (please refer to Table 3 for the related temperature and strain rate)

4.3.3 Rubbery plateau

In this section, we observed that the mechanical behaviour in the rubbery plateau were different dependent on the entanglement density of the PMMAs. For accounting such differences, we will focus in this section on PMMA 120 and PMMA 3500.

4.3.3.1 PMMA 120

Fig. 14 shows the contribution of each branch to the total stress for PMMA 120 at an equivalent strain rate of a) 10^{-2} s^{-1} (rubbery plateau) and b) 10^{-4} s^{-1} (near the flowing region) of this PMMA. For both equivalent strain rates, Branch 1 describes the initial regime and contributes to a relevant fraction of energy dissipation. This branch accounts for the viscoplastic-like behaviour (in the rubbery plateau) and plastic flow of the material at 10^{-2} s^{-1}. Notice that the strain at which Branch 1 stops to be less predominant decreases when passing from glassy to rubbery (10^{-2} s^{-1}) regime. Conversely, it increases again close when the flow region is reached (10^{-4} s^{-1}). At 10^{-2} s^{-1}, Branch 2 adds viscohyperelasticity and then turns into a viscoelastic network when reaching the flowing at 10^{-4} s^{-1}.

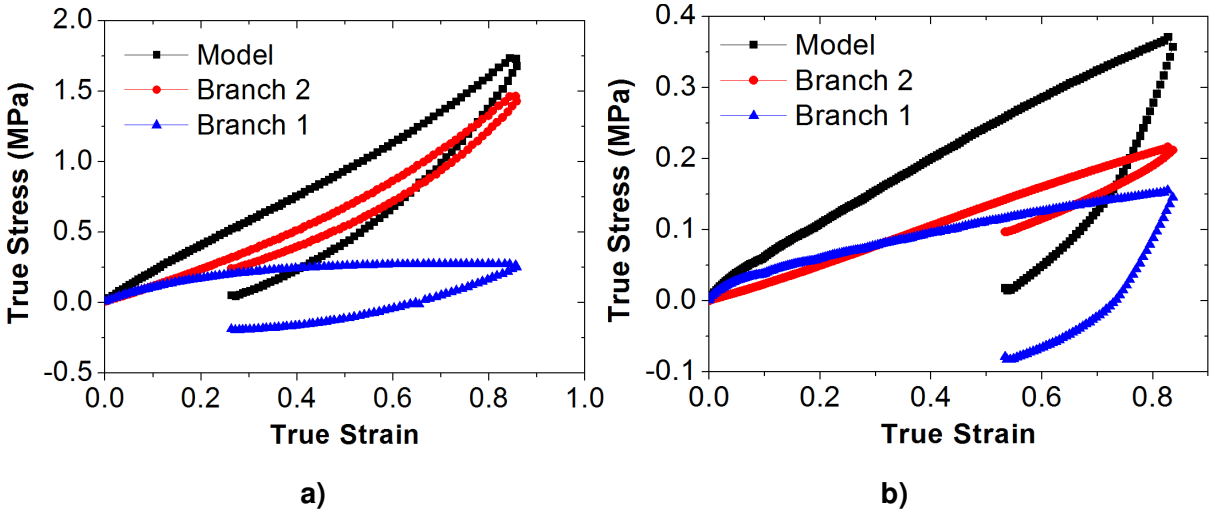

Fig.14: Contribution of each branch to the total stress-strain curves for PMMA 120 at 130 °C for equivalent strain rates of a) 10^{-2} s^{-1} and b) 10^{-4} s^{-1}. (please refer to Table 3 for the related temperature and strain rate)

4.3.3.2 PMMA 3500

Fig. 15 displays the contribution of each branch to the total stress for PMMA 3500 for an equivalent strain rate of a) 10^{-2} s^{-1} and b) 10^{-8} s^{-1}. This condition corresponds to the rubbery plateau of this PMMA. At 10^{-2} s^{-1}, Branch 1 still contributes to viscoplasticity by describing the initial elasticity and exhibiting energy dissipation. At 10^{-8} s^{-1}, the contribution of this branch becomes almost negligible. Additionally, Branch 2 exhibits a viscohyperelastic (with no much hysteresis) behaviour at 10^{-2} s^{-1}. Then, at 10^{-8} s^{-1}, the elastic and inelastic components of the mechanical response are described by

Branch 2 which displays viscohyperelastic behaviour with more hysteresis than at 10^{-2} s^{-1}. At this point, this branch can describe by itself the mechanical behaviour. Same results were observed for PMMA CL.

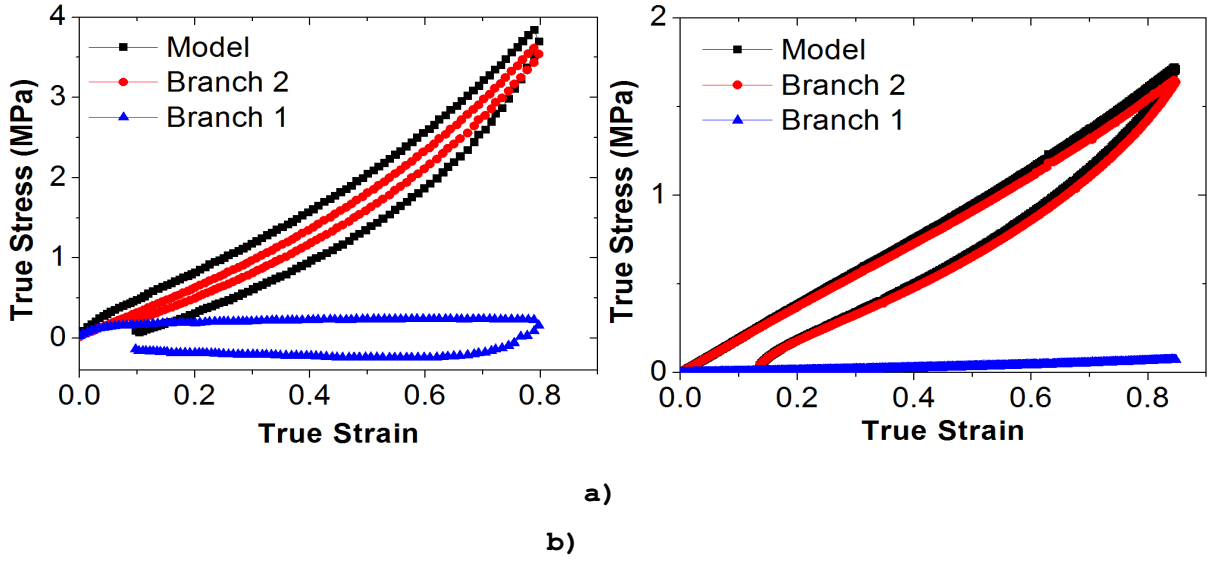

Fig. 15: Contribution of each branch to the total stress-strain curves for PMMA 3500 at 130 °C for equivalent strain rates of a) 10^{-2} s^{-1} and b) 10^{-8} s^{-1}. (please refer to Table 3 for the related temperature and strain rate)

Overall, considering a branch that accounts for viscoelasticity/viscoplasticity in parallel with a branch representing hyperelasticity/viscohyperelasticity, allows describing the mechanical response of amorphous PMMA at small and large deformation when submitted to non-monotonic tensile loading.

4.4 Dependence of the model's parameters with the equivalent strain rate

So far, we stated that the physical entanglements contribute to viscoelastoplastic behaviour while van der Waals interactions are more related to visco-hyperelastic or hyperelastic behaviour. However, entanglements and van der Waals interactions are likely dependent on the strain rate and temperature. Some authors proposed that such dependence could be described by an Eyring-like phenomenological approach [54]–[58] while other works proposed to relate these parameters to the equivalent strain rate at reference temperature by using a phenomenological sigmoid formulation [1], [2], [46]. By comparing both approaches, we found that a sigmoid function is more appropriate to describe the evolution of Ns_1^*, Nc_1^*, z, $p1$, Ns_2^* and α_2^2 with the equivalent strain rate:

$$\begin{Bmatrix} N_s^{1*} \\ N_c^{1*} \\ z \\ p_1 \\ N_s^{2*} \\ \alpha_2^2 \end{Bmatrix} = \begin{Bmatrix} N_{s0}^{1*} \\ N_{c0}^{1*} \\ z_0 \\ p_{10} \\ N_{s0}^{2*} \\ \alpha_{20}^2 \end{Bmatrix} + \begin{Bmatrix} N_{s1}^{1*} \\ N_{c1}^{1*} \\ z_1 \\ p_{11} \\ N_{s1}^{2*} \\ \alpha_{21}^2 \end{Bmatrix} \left(\frac{2}{1 + \left(\tau \dot{\varepsilon}_{eq} \right)^{-2m}} \right) \quad (15)$$

where, N_{s0}^{1*}, N_{c0}^{1*}, z_0, p_{10}, N_{s0}^{2*}, α_{20}^2, N_{s1}^{1*}, N_{c1}^{1*}, z_1, p_{11}, N_{s1}^{2*}, α_{21}^2, τ and m are material parameters. The parameters for fulfilling Equation (15) are presented in Table 4. The values τ=0.037 s^{-1} and m=0.375 were used for all cases. Fig. 16 displays the evolution of EV's parameter with the equivalent strain rate and the fitting of the sigmoid function. Results show that a sigmoid function is able to capture the evolution of the parameters over a wide range of equivalent strain rates. In addition, results suggest that parameters sharply increase with the equivalent strain rate when passing through α-transition and, more especially, Ns_1^*, z, $p1$ and Ns_2^*. Indeed, at short time scale (or low temperature), the density of entanglement and van der Waals interaction (Ns_1^* and Ns_2^*) seems to be more effective. Then, disentanglement parameters (z and $p1$), which rule the part of the energy dissipated by the polymer network under deformation, increase when the equivalent strain rate is higher. This is consistent with experimental observations. Therefore, these results show that the model accounts for a polymer network more rigid, dissipating more energy at high strain rates or low temperatures.

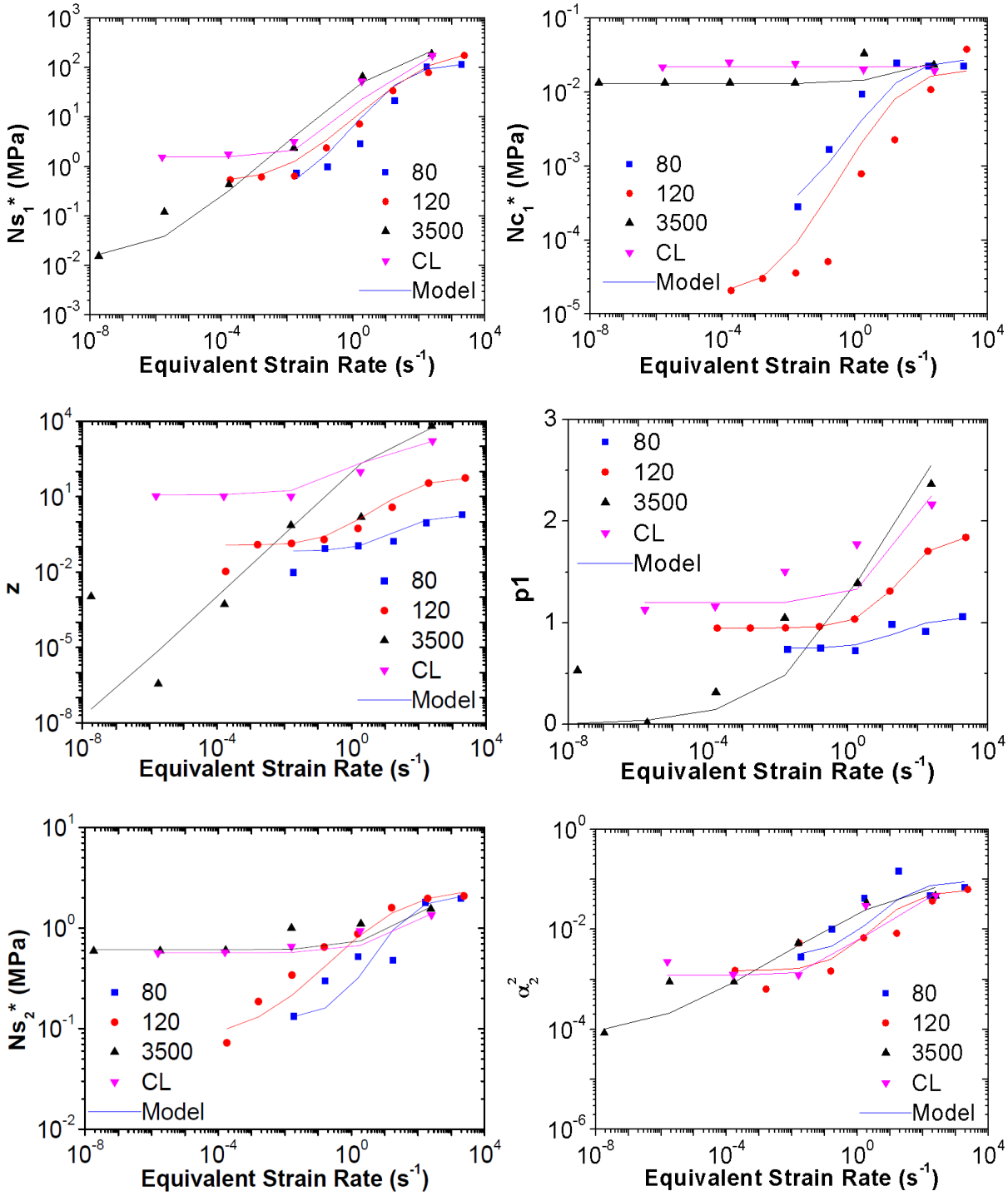

Fig. 16: Parameters evolution with the equivalent strain rate for PMMA 120 at reference temperature of 130 °C. From left to right and from top to bottom: Ns_1^*, Nc_1^*, z, $p1$, Ns_2^* and α_2^2.

Table 4: Phenomenological parameters identification for the different PMMAs.

	PMMA 80	**PMMA 120**	**PMMA 3500**	**PMMA CL**
N^1_{s0}*	0.300	0.500	0.015	1.560
N^1_{s1}*	60	75	140	100
N^1_{c0}*	$2x10^{-4}$	$2x10^{-5}$	0.013	0.022
N^1_{c1}*	0.014	0.010	0.007	$2x10^{-4}$
Z_0	0.070	0.120	$1x10^{-8}$	12
Z_1	0.770	29	3000	950
P_{10}	0.750	0.950	0.002	1.200
P_{11}	0.155	0.460	2.2	0.620
α^2_{20}	0.003	0.002	$8x10^{-5}$	0.001
α^2_{21}	0.045	0.030	0.049	0.030
N^2_{s0}*	0.125	0.080	0.610	0.570
N^2_{s1}*	1	1.200	0.600	0.480

For enriching the model capabilities, we coupled the constitutive model with the sigmoid evolution of the parameters of the Edward-Vilgis strain energy to account the strain rate/temperature effect on the mechanical response

This was tested on PMMA 120 and then compared to the original model (described in section 3). Fig. 17 displays this comparison for equivalent strain rates of 10^1 s^{-1} and 10^{-2} s^{-1}, respectively. We chose these conditions since the theoretical values differed the most with the sigmoid function (see Fig. 16). The differences between the original model and the coupling with the sigmoid function are quite small, around 2%, meaning that we can employ parameters for non-monotonic tensile loading of PMMAs of different molecular weight. These results are promising for future modelling since temperature and strain rate effects can be coupled into one parameter, equivalent strain rate at a reference temperature, by means of an empirical sigmoid function.

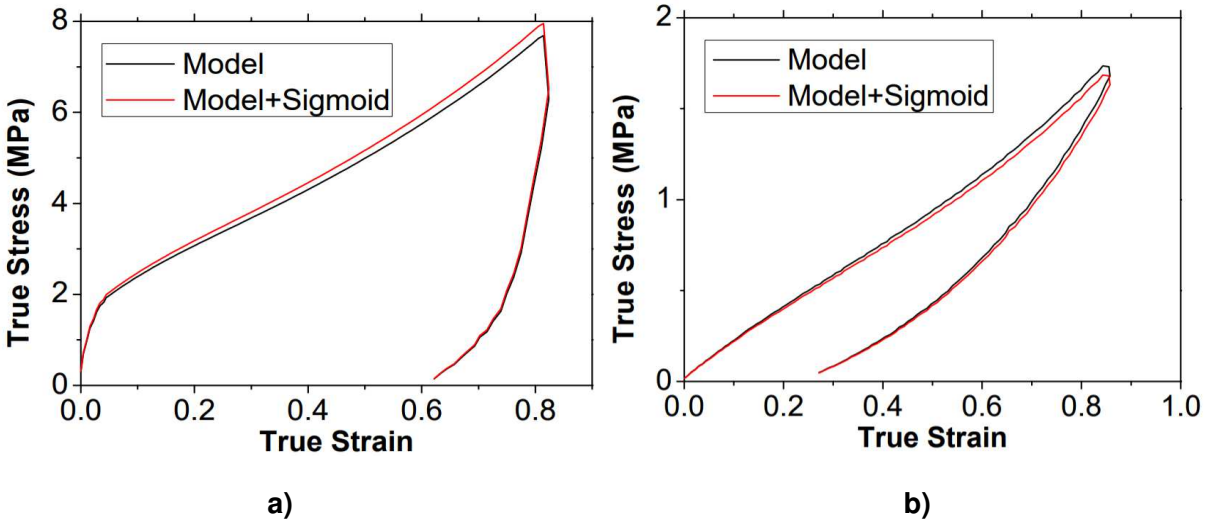

Fig. 17: Comparison between the initial model and the coupling with the sigmoid function on PMMA 120 at a) 10^{1} s^{-1} and b)10^{-2} s^{-1} at reference temperature of 130 °C. (please refer to Table 3 for the related temperature and strain rate used for these tests)

5 Conclusions

The purpose of this work was to verify the versatility of a model built on statistical chain network theory and inelasticity for capturing the main features of amorphous PMMAs with different molecular weights when tested under non-monotonic tensile loading. The constitutive model based on the approach proposed by [1], [2] and extended by [33] was calibrated with the experimental data of cyclic tensile tests for a large number of experimental conditions, going from the quasi-fluid state up to the glassy state while passing through the rubbery and viscoelastic regions. Reasonable agreement was observed between the theoretical results obtained with the model and the experimental data obtained for diverse PMMAs. More especially, the model exhibits capabilities to capture the different features of the material (viscoplasticity, viscoelasticity, hyperelasticity and viscohyperelasticity) at small and large deformations, while accounting for the contribution of the active physical entanglements, crosslinks and van der Waals interactions, and also of the inelastic mechanisms induced by disentanglements, evolution in the secondary bonds density and chain extensibility. Additionally, the sensitivity of the model parameters to the equivalent strain rate was accounted thanks to an empirical sigmoid function. Combining the sigmoid evolution with the initial model, allowed considering the time/temperature dependence on the constitutive modelling. Results present an acceptable agreement with the previous model.

In general, the versatility of the model reproducing different mechanical behaviours shows the efficiency of including the evolution of internal state variables while using Edward-Vilgis strain energy

function. The methodology presented in this work open new possibilities for modelling the mechanical response of polymers, and may enhance the numerical computations for predicting the material behaviour when studied in the viscoelastic and rubbery-like state.

Acknowledgments

The authors acknowledge the support of Pierre Gerard and Arkema for providing the material used in this study.

Annex 1

Table A1.1: Parameters for PMMA 80.and 120.

$\dot{\varepsilon}_{eq}$ (s^{-1})	Ns_1* (MPa)	Nc_1*x10^2 (MPa)	Z (-)	p1 (-)	Ns_2* (MPa)	α_2^2x10^2 (-)	τ_sx10^2 (-)	ξx10^2 (-)	v (-)	v'x10^3 (-)
PMMA 80										
0.02	0.74	0.03	0.01	0.76	0.13	0.29	33.1	64.0	1.71	250.0
0.17	1.02	0.17	0.09	0.76	0.30	1.03	7.75	45.9	2.30	16.30
1.61	2.92	0.95	0.11	0.73	0.52	4.28	9.17	42.8	6.90	0.727
18.1	21.6	2.51	0.17	0.99	0.49	1.50	21.2	71.7	0.14	0.077
169	105	2.27	0.91	0.92	1.80	4.81	1.77	0.004	0.09	0.001
1930	120	2.27	1.89	1.07	1.97	7.08	0.005	0.002	0.18	0.002
PMMA 120										
0.0002	0.54	0.002	0.01	0.75	0.07	0.15	29.4	97.9	3.18	112
0.0165	0.65	0.003	0.14	1.10	0.34	0.54	7.72	30.4	0.35	144
1.56	7.27	0.079	0.54	0.10	0.88	0.68	0.07	14.4	0.83	0.00
16.1	34.2	0.227	3.82	1.28	1.60	0.74	0.00	3.95	0.83	0.00
196	79.6	1.081	34.8	1.60	1.97	1.71	0.00	1.81	0.31	0.00
2390	177	7.791	56.0	1.78	2.09	6.33	0.00	0.02	1.17	0.00

Table A1.2: Parameters for PMMA 3500 and CL.

$\dot{\varepsilon}_{eq}$ (s^{-1})	Ns_1* (MPa)	Nc_1*x10^2 (MPa)	Z (-)	p1 (-)	Ns_2* (MPa)	α_2^2x10^2 (-)	τ_sx10^3 (-)	ξ (-)	v (-)	v'x10^3 (-)
PMMA 3500										
1.84x10^{-8}	0.016	1.34	0.001	0.53	0.59	0.01	521.0	0.52	0.12	2.52
1.82x10^{-6}	0.121	1.34	0.000	0.02	0.60	0.09	101.0	0.61	6.90	17.8
1.68x10^{-4}	0.433	1.34	0.001	0.32	0.60	0.09	0.346	0.19	0.66	4.58
1.58x10^{-2}	2.40	1.34	0.733	1.05	1.00	0.53	0.224	0.13	0.76	17.1
1.92	65.8	3.34	1.550	1.39	1.10	3.43	0.022	0.17	0.12	8.38
244	189	3.34	6585	2.37	1.55	4.71	0.258	0.00	0.02	0.00
PMMA CL										
1.56x10^{-6}	1.56	2.17	10.8	1.13	0.56	0.23	0.005	1.25	0.0003	0.022
1.61x10^{-4}	1.79	2.51	10.6	1.16	0.58	0.12	0.008	1.42	0.0002	0.035
1.59x10^{-2}	3.18	2.42	10.2	1.51	0.66	0.12	0.008	1.65	0.0000	0.029
1.83	52.7	2.01	98.3	1.78	0.94	3.02	0.054	1.37	0.0926	0.011
255	174	1.93	1664	2.16	1.35	4.80	0.408	0.00	0.0142	0.008

Annex 2

Calculation for equivalent Young, E, associated to Edward Vilgis' model:

Let's F be the potential of a medium submitted to an uniaxial extension λ. According to initial model, on can write F as:

$$F = \frac{kTN}{2}\left\{\begin{array}{c}\dfrac{(1+\eta)(1-\alpha^2)}{(1-\alpha^2 C)}\left(\dfrac{\lambda^2}{A}+\dfrac{2}{B}\right)\\ +\ln(A)+2\ln(B)-2\ln(\lambda)+\ln(1-\alpha^2 C)\end{array}\right\}$$

$$A = 1+\eta\lambda^2; \qquad \frac{\partial A}{\partial \lambda} = 2\eta\lambda;$$

$$B = \lambda+\eta; \qquad \frac{\partial B}{\partial \lambda} = 1;$$

$$C = \lambda^2+\frac{2}{\lambda}; \qquad \frac{\partial C}{\partial \lambda} = 2\lambda-\frac{2}{\lambda^2}; \qquad \text{(A1)}$$

where *N*, $\alpha^2$and η are the density of entanglements, the extensibility of chains and the freedom of entanglements, respectively.

Let's define the modulus as the mathematical limiting slope for zero strain of the stress, σ, vs. strain, ε as written in Eq. (A2).

$$E = \lim_{\varepsilon\to 0}\frac{\partial \sigma}{\partial \varepsilon} = \lim_{\lambda\to 1}\lambda\frac{\partial \sigma}{\partial \lambda} \qquad \text{(A2)}$$

For its part, the axial stress in a 1D assumption is given by:

$$\sigma = \lambda\frac{\partial F}{\partial \lambda} \qquad \text{(A3)}$$

Then from Eq. (A1) and (A3) one can conclude on Eq. (A4):

$$\frac{\partial F}{\partial \lambda} = \frac{kTN}{2}\left\{\begin{array}{c}\dfrac{(1+\eta)(1-\alpha^2)}{(1-\alpha^2 C)}\left(\dfrac{2\lambda}{A}-\dfrac{\lambda^2}{A^2}\dfrac{\partial A}{\partial \lambda}-\dfrac{2}{B^2}\dfrac{\partial B}{\partial \lambda}\right)\\ +\dfrac{(1+\eta)(1-\alpha^2)}{(1-\alpha^2 C)^2}\left(\dfrac{\lambda^2}{A}+\dfrac{2}{B}\right)\alpha^2\dfrac{\partial C}{\partial \lambda}\\ +\dfrac{1}{A}\dfrac{\partial A}{\partial \lambda}+\dfrac{2}{B}\dfrac{\partial B}{\partial \lambda}-\dfrac{2}{\lambda}-\dfrac{\alpha^2}{(1-\alpha^2 C)}\dfrac{\partial C}{\partial \lambda}\end{array}\right\}$$

$$A = 1+\eta\lambda^2; \qquad \frac{\partial A}{\partial \lambda} = 2\eta\lambda;$$

$$B = \lambda+\eta; \qquad \frac{\partial B}{\partial \lambda} = 1;$$

$$C = \lambda^2 + \frac{2}{\lambda}; \qquad \frac{\partial C}{\partial \lambda} = 2\lambda - \frac{2}{\lambda^2}; \tag{A4}$$

The axial stress is then:

$$\lambda \frac{\partial F}{\partial \lambda} = \sigma = \frac{kTN}{2} \left\{ \begin{array}{c} \frac{(1+\eta)(1-\alpha^2)}{(1-\alpha^2 C)} \left(\frac{2\lambda^2}{A^2} - \frac{2\lambda}{B^2} \right) \\ + \frac{(1+\eta)(1-\alpha^2)}{(1-\alpha^2 C)^2} \left(\frac{\lambda^2}{A} + \frac{2}{B} \right) \alpha^2 \left(2\lambda^2 - \frac{2}{\lambda} \right) \\ + \frac{2\eta\lambda^2}{A} + \frac{2\lambda}{B} - 2 - \frac{\alpha^2}{(1-\alpha^2 C)} \left(2\lambda^2 - \frac{2}{\lambda} \right) \end{array} \right\}$$

$$A = 1 + \eta\lambda^2; \qquad \frac{\partial A}{\partial \lambda} = 2\eta\lambda; \qquad \lambda \frac{\partial A}{\partial \lambda} = 2\eta\lambda^2 = 2A - 2;$$

$$B = \lambda + \eta; \qquad \frac{\partial B}{\partial \lambda} = 1;$$

$$C = \lambda^2 + \frac{2}{\lambda}; \qquad \frac{\partial C}{\partial \lambda} = 2\lambda - \frac{2}{\lambda^2}; \tag{A5}$$

The derivative of the stress results is:

$$\frac{\partial \sigma}{\partial \lambda} = 3kTN \left\{ \begin{array}{c} \frac{(1-\alpha^2)}{(1-3\alpha^2)} \left(\frac{1-\eta}{(1+\eta)^2} \right) \\ +3 \frac{(1-\alpha^2)}{(1-3\alpha^2)^2} \alpha^2 + \frac{\eta}{(1+\eta)^2} - \frac{\alpha^2}{(1-3\alpha^2)} \end{array} \right\} \tag{A6}$$

Finally:

$$E = 3kTN \left\{ \frac{(1-\alpha^2-2\eta\alpha^2)}{(1-3\alpha^2)(1+\eta)^2} + \frac{2\alpha^2}{(1-3\alpha^2)^2} \right\} \tag{A7}$$

6 References

[1] N. Billon, “New Constitutive Modeling for Time-Dependent Mechanical Behavior of Polymers Close to Glass Transition : Fundamentals and Experimental Validation,” *J. Appl. Polym. Sci.*, 2012.

[2] A. Maurel-Pantel, E. Baquet, J. Bikard, J. L. Bouvard, and N. Billon, “A thermo-mechanical large deformation constitutive model for polymers based on material network description: Application to a semi-crystalline polyamide 66,” *Int. J. Plast.*, vol. 67, pp. 102–126, Apr. 2015.

[3] J. L. Bouvard, D. K. Ward, D. Hossain, S. Nouranian, E. B. Marin, and M. F. Horstemeyer, “Review of Hierarchical Multiscale Modeling to Describe the Mechanical Behavior of Amorphous Polymers,” *J. Eng. Mater. Technol.*, vol. 131, 2009.

[4] C. G’Sell and J. J. Jonas, “Determination of the plastic behavior of solid polymers at constant true strain rate,” *J. Mater. Sci.*, vol. 14, pp. 583–591, 1979.

[5] C. G’Sell and J. M. Haudin, *Lois de comportement mécanique des polymères solides. Introduction à la mécanique des polymères*. 1995.

[6] S. G. Bardenhagen, M. G. Stout, and G. T. Gray, “Three-Dimensional Finite Deformation Viscoplastic Constitutive Models for Polymeric Materials,” *Mech. Mater.*, vol. 25, pp. 235–253, 1997.

[7] V. A. Lubarda, D. J. Benson, and M. A. Meyers, “Strain-Rate Effects in Rheological Models of Inelastic Response,” *Int. J. Plast.*, vol. 19, pp. 1097–118, 2003.

[8] N. Billon, “Effet de couplage thermomécanique dans la caractérisation du comportement de polymères solides,” *Mécanique Ind.*, vol. 4, pp. 357–364, 2003.

[9] A. S. Khan, O. Lopez-Pamies, and R. Kasmi, “Thermo-mechanical large deformation response and constitutive modeling of viscoelastic polymers over a wide range of strain rates and temperatures,” *Int. J. Plast.*, vol. 22, pp. 581–601, 2006.

[10] H. Wang, H. Zhou, Z. Huang, Y. Zhang, and X. Zhao, “Constitutive modeling of polycarbonate over a wide range of strain rates and temperatures,” *Mech. Time-Dependent Mater.*, vol. 21, pp. 97–117, 2017.

[11] O. A. Hasan and M. C. Boyce, “A Constitutive Model for the Nonlinear Viscoelastic Viscoplastic Behavior of Glassy-Polymers,” *Polym. Eng. Sci.*, vol. 35, no. 4, pp. 331–344, 1995.

[12] A. Muliana, K. R. Rajagopal, D. Tscharnuter, and G. Pinter, “A nonlinear viscoelastic constitutive model for polymeric solids based on multiple natural configuration theory,” *Int. J. Solids Struct.*, vol. 100–101, pp. 95–110, 2016.

[13] J. Guo *et al.*, “A thermodynamics viscoelastic constitutive model for shape memory polymers,” *J. Alloys Compd.*, vol. 705, pp. 146–155, 2017.

[14] C. Yu, G. Kang, K. Chen, and F. Lu, “A thermo-mechanically coupled nonlinear viscoelastic–viscoplastic cyclic constitutive model for polymeric materials,” *Mech. Mater.*, vol. 105, pp. 1–15, 2017.

[15] Y. Li, Y. He, and Z. Liu, “A viscoelastic constitutive model for shape memory polymers based on multiplicative decompositions of the deformation gradient,” *Int. J. Plast.*, vol. 91, pp. 300–317, 2017.

[16] J. Gu, J. Leng, and H. Sun, “A constitutive model for amorphous shape memory polymers based on thermodynamics with internal state variables,” *Mech. Mater.*, vol. 111, pp. 1–14, 2017.

[17] F. Praud, G. Chatzigeorgiou, J. Bikard, and F. Meraghni, “Phenomenological multi-mechanisms constitutive modelling for thermoplastic polymers, implicit implementation and experimental validation,” *Mech. Mater.*, vol. 114, pp. 9–29, 2017.

[18] C. P. Buckley and D. C. Jonest, “Glass-rubber constitutive model for amorphous polymers near the glass transition,” *Polymer*, vol. 36, pp. 3301–3312, 1995.

[19] C. P. Buckley and D. C. Jonest, “Hot-drawing of poly (ethylene terephthalate) under biaxial stress: application of a three-dimensional glass-rubber constitutive model,” *Polymer*, vol. 37, pp. 2403–2414, 1996.

[20] P. J. Dooling, C. P. Buckley, S. Rostami, and N. Zahlan, “Hot-drawing of poly(methyl methacrylate) and simulation using a glass - Rubber constitutive model,” *Polymer*, vol. 43, pp. 2451–2465, 2002.

[21] J. Sweeney, R. Spares, and M. Woodhead, “A Constitutive Model for Large Multiaxial Deformations of Solid Polypropylene at High Temperature,” *Polym. Eng. Sci.*, vol. 49, pp. 1902–1908, 2009.

[22] R. Dupaix and M. C. Boyce, “Constitutive modeling of the finite strain behavior of amorphous polymers in and above the glass transition,” *Mech. Mater.*, vol. 39, pp. 39–52, 2007.

[23] G. Ayoub, F. Zaïri, M. Naït-Abdelaziz, and J. M. Gloaguen, “Modelling large deformation behaviour under loading-unloading of semicrystalline polymers: Application to a high density polyethylene,” *Int. J. Plast.*, vol. 26, no. 3, pp. 329–347, 2010.

[24] E. M. Arruda and M. C. Boyce, “A three-dimensional constitutive model for the large stretch behavior of rubber elastic materials,” *J. Mech. Phys. Solids*, vol. 41, pp. 389–412, 1993.

[25] J. S. Bergstrom and M. C. Boyce, “Constitutive modeling of the large strain time-dependent behavior of elastomers,” *J. Mech. Phys. Solids*, vol. 46, pp. 931–954, 1998.

[26] M. C. Boyce, S. Socrate, and P. G. Llana, “Constitutive model for the finite deformation stress–strain behavior of poly(ethylene terephthalate) above the glass transition,” *Polymer*, vol. 41, pp. 2183–2201, 2000.

[27] O. U. Colak, “Modeling deformation behavior of polymers with viscoplasticity theory based on overstress,” *Int. J. Plast.*, vol. 21, pp. 145–160, 2005.

[28] L. Anand, N. M. Ames, V. Srivastava, and S. A. Chester, “A thermomechanically coupled theory for large deformations of amorphous polymers. part I: Formulation,” *Int. J. Plast.*, vol. 25, pp. 1474–1494, 2009.

[29] N. M. Ames, V. Srivastava, S. A. Chester, and L. Anand, “A thermomechanically coupled theory for large deformations of amorphous polymers. part II: Applications,” *Int. J. Plast.*, vol. 25, pp. 1495–1539, 2009.

[30] V. Srivastava, S. A. Chester, N. M. Ames, and L. Anand, “A thermo-mechanically-coupled large-deformation theory for amorphous polymers in a temperature range which spans their glass transition,” *Int. J. Plast.*, vol. 26, no. 8, pp. 1138–1182, 2010.

[31] A. N. Gent, “A new constitutive relation for rubber,” *Rubber Chem. Technol.*, vol. 69, pp. 59–61, 1996.

[32] S. F. Edwards and T. Vilgis, “The effect of entanglements in rubber elasticity,” *Polymer*, vol. 27, pp. 483–492, 1986.

[33] F. Gehring, J.-L. Bouvard, and N. Billon, “Modeling of time dependent mechanical behavior of polymers: Comparison between amorphous and semicrystalline polyethylene terephthalate,” *J. Appl. Polym. Sci.*, vol. 133, no. 35, pp. 1–17, Sep. 2016.

[34] C. E. Federico, J. L. Bouvard, C. Combeaud, and N. Billon, “Large strain/time dependent mechanical behaviour of PMMAs of different chain architectures. Application of time-temperature superposition principle,” *Polymer*, vol. 139, pp. 177–187, 2018.

[35] M. A. Sutton, J.-J. Orteu, and H. W. Schreier, *Image Correlation for Shape, Motion and Deformation Measurements: Basic Concepts, Theory and Applications*. Springer.

[36] F. Grytten, H. Daiyan, M. Polanco-Loria, and S. Dumoulin, “Use of digital image correlation to measure large-strain tensile properties of ductile thermoplastics,” *Polym. Test.*, vol. 28, no. 6, pp. 653–660, Sep. 2009.

[37] N. Candau, C. Pradille, J. L. Bouvard, and N. Billon, “On the use of a four-cameras stereovision system to characterize large 3D deformation in elastomers,” *Polym. Test.*, vol. 56, no. October, pp. 314–320, 2016.

[38] I. Eshraghi, M. R. Y. Dehnavi, and N. Soltani, “Effect of Subset Parameters Selection on the Estimation of Mode-I Stress Intensity Factor in a Cracked PMMA Specimen using Digital Image Correlation,” *Polym. Test.*, no. August, 2014.

[39] H. Schreier, J. Braasch, and M. Sutton, “Systematic errors in digital image correlation caused by intensity interpolation,” *Opt. Eng.*, vol. 39, no. 11, 2000.

[40] V. P. Zok, M. N. Rajan, and W. F. Rossol, “Optimization of Digital Image Correlation for High-Resolution Strain Mapping of Ceramic Composites,” *Exp. Mech.*, pp. 1407–1421, 2012.

[41] N. Billon, “Constitutive model for HIPS in the thermoforming range,” *Int. J. Mater. Form.*, vol. 1, no. S1, pp. 679–682, Apr. 2008.

[42] C. G. Sell, J. M. Hiver, and A. Dahoun, “Experimental characterization of deformation damage in solid polymers under tension, and its interrelation with necking,” *Int. J. Solids Struct.*, vol. 39, pp. 3857–3872, 2002.

[43] J. Diani, P. Gilormini, and J. S. Arrieta, “Direct experimental evidence of time-temperature superposition at fi nite strain for an amorphous polymer network,” *Polymer*, vol. 58, pp. 107–112, 2015.

[44] J. D. Ferry, *Viscoelastic Properties of Polymers*, 3rd ed. New York: John Wiley & Sons, 1980.

[45] E. Baquet, “Modélisation thermomécanique visco-hyperélastique du comportement d’un polymère semi-cristallin : application au cas d’une matrice polyamide 6.6,” Ecole Nationale Supérieur des Mines de Paris, 2011.

[46] J. Sweeney, “A constitutive law for large deformations of polymers at high temperatures,” *J. Mech. Phys. Solids*, vol. 44, pp. 1033–1049, 1996.

[47] A. M. Adams, C. P. Buckley, and D. P. Jones, “Biaxial hot drawing of poly(ethylene terephthalate): Measurements and modelling of strain-stiffening,” *Polymer*, vol. 41, pp. 771–786, 2000.

[48] J. . Wu and C. P. Buckley, “Plastic deformation of glassy polysterene: a unified model of yield and the role of chain length,” *J. Polym. Sci. Part B*, vol. 42, pp. 2027–2040, 2004.

[49] A. C.-Y. Lew and C. P. Buckley, “Biaxial constitutive response of PET during hot drawing: Experimental study and new implications for constitutive modelling,” *Annual Technical Conference - ANTEC, Conference Proceedings*, vol. 4, Pages. pp. 2294–2298, 2007.

[50] E. Gorlier, “Caractérisation rhéologique et structurale d’un PET. Application au procédé de bi-étirage soufflage de bouteilles,” Ecole Nationale Supérieure des Mines de Paris, 2001.

[51] R. Ball, M. Doi, S. F. Edwards, and M. Warner, “Elasticity of entangled networks,” *Polymer*, vol. 22, 1981.

[52] J. A. Nelder and R. Mead, “A simplex method for function minimization,” *Comput. J.*, vol. 7, pp. 308–313, 1965.

[53] J. C. Lagarias, J. A. Reeds, M. H. Wright, and P. E. Wright, “Convergence properties of the nelder–mead simplex method in low dimensions,” *SIAM J. Optim.*, vol. 9, no. 1, 1998.

[54] J. Sweeney and I. M. Ward, “Rate dependent and network phenomena in the multiaxial drawing of poly(vinyl chloride),” *Polymer*, vol. 36, pp. 299–308, 1995.

[55] J. Sweeney, T. L. D. Collins, P. D. Coates, and I. M. Ward, “Application of an elastic model to the large deformation, high temperature stretching of polypropylene,” *Polymer*, vol. 38, pp. 5991–5999, 1997.

[56] R. G. Matthews, R. A. Duckett, I. M. Ward, and D. P. Jones, “The biaxial drawing behaviour of poly(ethylene terephthalate),” *Polymer*, vol. 38, no. 19, pp. 4795–4802, 1997.

[57] E. Gorlier, J. F. Agassant, J. M. Haudin, and N. Billon, “Experimental and theoretical study of uniaxial deformation of amorphous poly(ethylene terephthalate) above glass transition temperature,” *Plast. Rubber Compos.*, vol. 30, 2001.

[58] J. Johnsen, F. Grytten, O. S. Hopperstad, and A. H. Clausen, “Influence of strain rate and temperature on the mechanical behaviour of rubber-modified polypropylene and cross-linked polyethylene,” *Mech. Mater.*, vol. 114, pp. 40–56, 2017.

[59] J. Wang, L.F. Peng, Y.J. Deng, X.M. Lai, M.W. Fu, J. Ni, "A finite strain thermodynamically-based constitutive modeling and analysis of viscoelastic-viscoplastic deformation behavior of glassy polymers, International Journal of Plasticity, Vol. 122, pp. 135-163, 2019.

[60] J. Johnsen, A. H. Clausen, F. Grytten, A. Benallal, O. S. Hopperstad, "A thermo-elasto-viscoplastic constitutive model for polymers", Journal of the Mechanics and Physics of Solids, Vol. 124, pp. 681-701, 2019.

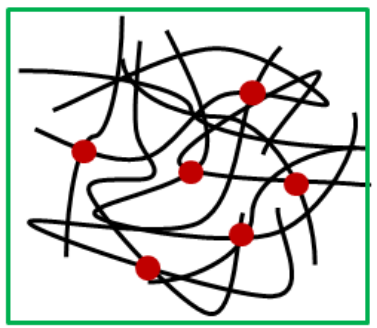

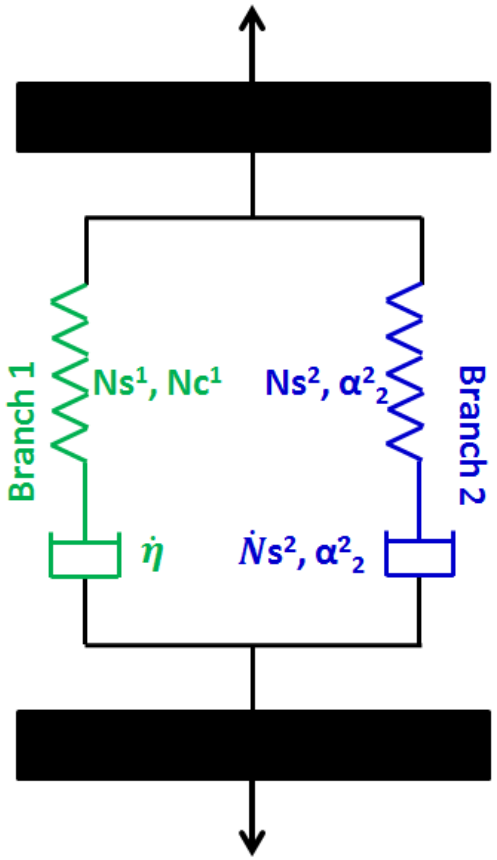
Branch 1
Ns¹, Nc¹
Ns², α²₂
Branch 2
η̇
Ṅs², α²₂

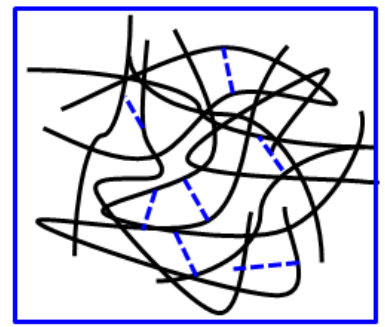

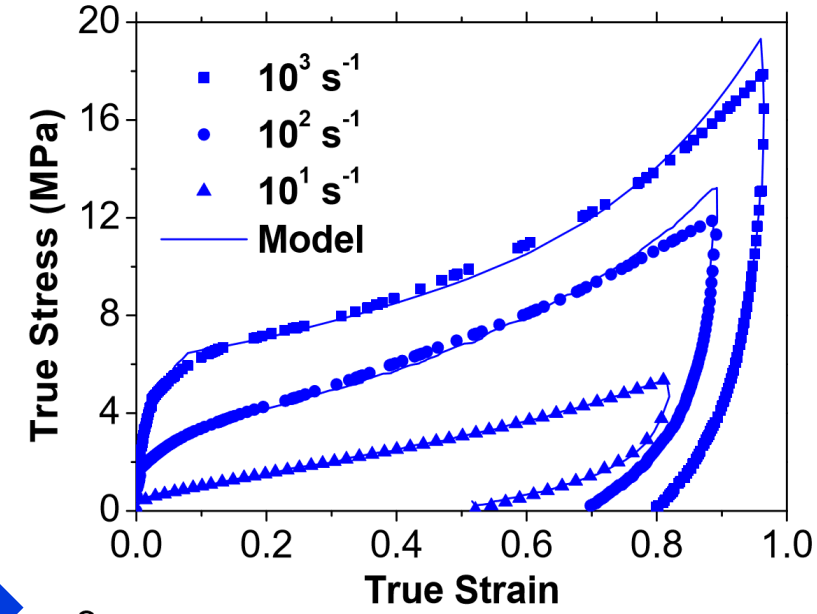
10³ s⁻¹
10² s⁻¹
10¹ s⁻¹
Model
True Stress (MPa)
True Strain
0
4
8
12
16
20
0.0
0.2
0.4
0.6
0.8
1.0

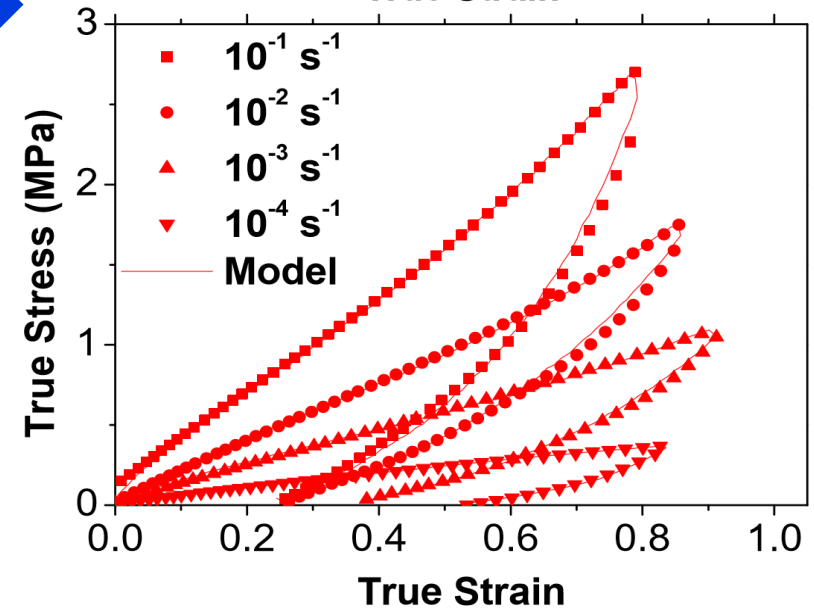
10⁻¹ s⁻¹
10⁻² s⁻¹
10⁻³ s⁻¹
10⁻⁴ s⁻¹
Model
True Stress (MPa)
True Strain
0
1
2
3
0.0
0.2
0.4
0.6
0.8
1.0